KU LEUVEN

FACULTEIT INGENIEURSWETENSCHAPPEN

Correlation of multiparametric, quantitative MRI with histology for tumor grading in prostate cancer

Daan Belmans

Thesis submitted to obtain the degree of Master of Science in Biomedical Engineering

Promotors:

Prof. Dr. Ir. Frederik Maes

Prof. Dr. Ir. Uwe Himmelreich

Mentor:

Dr. Ir. Janaki Raman Rangarajan

Academic year 2017 – 2018

Preface

The KU Leuven's faculty of Engineering calls the thesis project 'the icing on the cake of the master program'. Well, I am glad to admit that it was indeed a very challenging, yet nice experience.

I want to thank my promotors Prof. Dr. Ir. Frederik Maes and Prof. Dr. Ir. Uwe Himmelreich for having me on this very interesting thesis topic. It was amazing to work in this diverse environment on a real-life project and to be part of a real research group. Prof. Himmelreich was a great help during the ex-vivo data acquisition and was always there to provide instructions regarding the scanner software. Also thanks to Dr. Willy Gsell for transferring the ex-vivo scans to the drive. Prof. Maes pointed out the main directions of the thesis. I was always welcome to discuss problems and questions. His advice was of major use and was well appreciated.

The next person that deserves credit is the mentor of this thesis: Dr. Ir. Janaki Raman Rangarajan. Although less available in the second semester due to a change of job, he was a tremendous help in the first semester. Always eager to solve my problems and more than only guide me, he wanted to sincerely help me. Also for the finalization of the thesis, he gave some very useful advice. I wish him the best of luck in his new job!

Special thanks goes out to Cédric Draulans, a PhD in Radiotherapy with whom I cooperated a lot. He was responsible for the in-vivo image workflow and executed most of the registrations. We helped each other well and without him, the results of my thesis would probably not be what they are now.

Lastly, I want to thank friends and family for mental support and for revising my text. The final result would not be the same without them.

Daan Belmans

Contents

Abstract

Background: Whereas multiparametric magnetic resonance imaging (mp-MRI) is a promising technique for non-invasive detection and monitoring of prostate cancer, it needs further validation. In this work, a workflow was established for processing of in-vivo and ex-vivo acquired imaging data and to correlate these with histology. This allowed to quantify the in-vivo and ex-vivo apparent diffusion coefficient (ADC) and ex-vivo T2-relaxation time for tumor and healthy prostate tissue based on an histological ground-truth. In addition, the influence of fixation time, magnetic field strength of the ex-vivo scanner and tissue malignancy on the quantified T2- and ADC-values was investigated.
Materials and methods: For fifteen patients that underwent radical prostatectomy, in-vivo mp-MRI images were registered to histology images with delineated tumor regions, facilitated by high-resolution ex-vivo mp-MRI, using a patient-specific 3D prostate mold. Ex-vivo specimens were scanned on a 7T and/or 9.4T scanning device and three were scanned at multiple fixation times. Ex-vivo diffusion-weighted imaging (DWI) was done for different numbers of directions and b-values. Average T2- and ADC-values were calculated slice by slice for peripheral (PZ) and transition zone (TZ) tumor and non-tumor regions. Small tumor regions were excluded to minimize partial volume effects and the influence of small registration errors.
Results: In-vivo and ex-vivo ADC-values, expressed in $10^{-3}mm^2/s$, were significantly lower in tumor compared to non-tumor regions, in the PZ (1.24 ± 0.18 vs 1.45 ± 0.15 in-vivo, 0.50 ± 0.17 vs 0.62 ± 0.15 ex-vivo) as well as in the TZ (1.31 ± 0.26 vs 1.55 ± 0.20 in-vivo, 0.50 ± 0.15 vs 0.76 ± 0.16 ex-vivo). Ex-vivo T2-values, expressed in ms, were neither in the PZ nor in the TZ significantly different in tumor compared to non-tumor regions (31.62 ± 7.22 vs 29.06 ± 4.22 for the PZ, 31.11 ± 3.42 vs 32.10 ± 4.11 for the TZ). T2- and ADC-values decreased rapidly immediately after fixation, but this downward trend diminished for longer fixation times (especially for ADC-values). ADC-values were significantly lower when higher b-values were used for DWI due to bi-exponential diffusion decay. Whereas ADC-values did not change with field strength, T2-values for field strengths above 7T dropped significantly due to microscopic diffusion and susceptibility effects.
Conclusions: This study contributes to exploiting the potential of mp-MRI, and more in particular ADC-mapping, to distinguish tumor from non-tumor tissue in prostate cancer. Furthermore, the possible impact of fixation time, magnetic field strength and DWI protocol on the quantification of T2- and/or ADC-values was investigated such that these factors can be accounted for in future studies.

List of Figures

List of Tables

List of Abbreviations

PSA	Prostate-Specific Antigen
Mp-MRI	Multiparametric Magnetic Resonance Imaging
T2w-MRI	T2-weighted Magnetic Resonance Imaging
DWI	Diffusion-weighted Imaging
DCE imaging	Dynamic Contrast-Enhanced imaging
MRS	Magnetic Resonance Spectroscopy
ADC	Apparent Diffusion Coefficient
CZ	Central Zone
TZ	Transition Zone
PZ	Peripheral Zone
DRE	Digital Rectal Exam
AFS	Anterior Fibromuscular Stroma
TRUS	Transrectal Ultrasound
TNM	Tumor-Node-Metastasis
AJCC	American Joint Committee on Cancer
cT	clinical T-stage
pT	pathological T-stage
EBR	External Beam Radiation
CT	Computed Tomography
ADT	Androgen Deprivation Therapy
RF	Radio-frequent
TR	Repetition Time
TE	Echo Time
SSFSE	Single-Shot Fast Spin-Echo
PGSE	Pulsed Gradient Spin-Echo
SNR	Signal-to-Noise Ratio
DTI	Diffusion Tensor Imaging
FA	Fractional Anisotropy
Rwo	Rate of wash out
STEAM	Stimulated Echo Acquisition Mode
IAUC	Initial Area Under the Curve

mESD	multi-Exponential Signal Decay
RARE	Rapid imaging with Refocused Echoes
SE	Spin-Echo
FLASH	Fast Low Angle Shot
MoSAIC	Molecular Small Animal Imaging Centre
DICOM	Digital Imaging and Communications in Medicine
TIFF	Tagged Image File Format
stl	surface tessellation language
cso	contour segmentation objects
ROI	Region Of Interest
NN	Nearest Neighbour

Chapter 1

Introduction

Prostate cancer is the most prevalent type of cancer among men in Western countries: one man out of seven will encounter the disease in his life [1][2]. Diagnosis occurs mostly at an older age, with an average age of 66 [3]. Prostate cancer usually develops slowly and thanks to early detection and accurate therapeutic intervention, there is an observed reduction in mortality. Yet, the disease is the fifth leading cause of cancer deaths in men, with still a total of 307 000 worldwide deaths in 2012 [4]. It is therefore of utmost importance to optimize the current diagnostic methods to further lower the mortality rate [3][5]. Current procedures for detecting prostate cancer involve amongst others prostate-specific antigen (PSA) screening and ultrasound guided biopsies [6]. Both methods are however invasive since PSA-testing includes a blood test and biopsies involve tissue sampling with a needle. Furthermore, these techniques lack sensitivity and specificity. It is therefore essential to keep track on developing new techniques towards detection, evaluation and monitoring of prostate cancer, preferably in a non-invasive way.

Multiparametric magnetic resonance imaging (mp-MRI) has great potential to this end: it consists of conventional T2-weighted MRI (T2w-MRI), diffusion-weighted imaging (DWI), dynamic contrast-enhanced (DCE) imaging and magnetic resonance spectroscopy (MRS) [5]. On top of anatomical information, it thus also provides functional information on the diffusion, perfusion and metabolic characteristics of soft tissues. Conventional medical imaging techniques allow to detect the presence or absence of a tumor and to assess its extent. Combining the quantitative information of mp-MRI however, may additionally enable to assess the aggressiveness of the tumor tissue in a non-invasive way. In this way, it can mean a great added value for the current screening techniques. One application lies in the potential for more accurate biopsies. Mp-MRI can be used to identify regions that are highly suspicious of being malignant. These 'hotspots' can then be targeted in a biopsy, rather than to take samples from random regions of the prostate. Another application involves an improved treatment planning. Newer treatment methods are evolving towards a more local treatment, leaving the surrounding healthy tissue unharmed. To be sure however that the entire tumor is targeted by the treatment procedure, a precise

assessment of the malignant region is required. This can be done by mp-MRI. Additionally, since mp-MRI is non-invasive, it may be more convenient for the patient when extensive follow-up is needed. A third application, which is the focus of the study wherein this thesis is situated, aims to establish a parameter set from mp-MRI that is able to quantify the aggressiveness of cancerous tissue. More specifically, it focuses on the use of the apparent diffusion coefficient (ADC), obtained from DWI, and of the T2-relaxation time, obtained from T2w-MRI, to improve the grading of prostate tumors based on histological images as ground-truth. In order to be able to construct a set of MRI parameters that correlates with histologically defined tumor aggressiveness, in-vivo images need to be accurately compared to the histology images of excised prostate specimens. This implies that the histology images are properly aligned or registered to the in-vivo images, such that an histological ground-truth about the presence or absence of tumor or its grade is available for the entire prostate region in the in-vivo images.

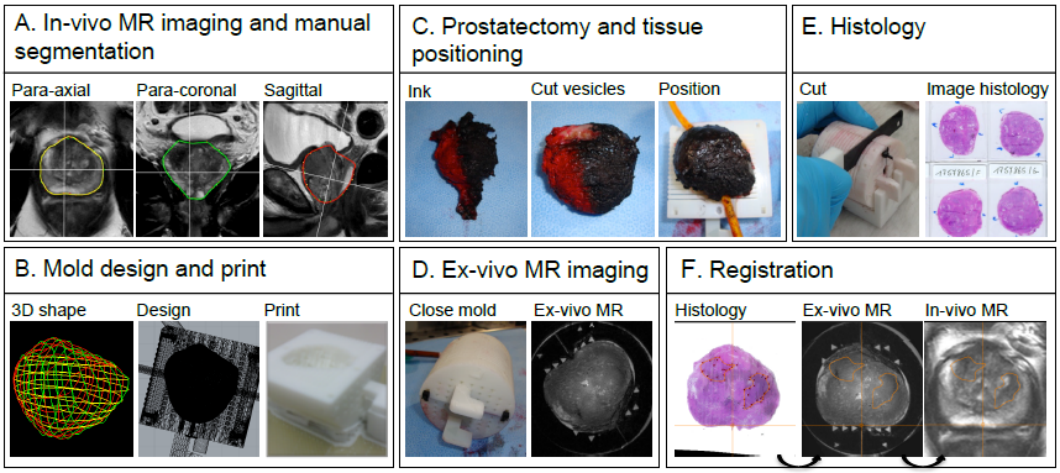

Figure 1.1: Workflow used in the present project to register in-vivo MRI-images to histology images. Ex-vivo images are used as an intermediate step and a patient-specific mold facilitates in-vivo to ex-vivo registration [7].

Histology to in-vivo MRI registration is however complicated by the usually low out-of-plane resolution of in-vivo images [7]. Moreover, histology images and MRI-images contain different information and there is a lack of 3D information, such that possible differences in slice orientation cannot be corrected for. To resolve these issues, a patient-specific 3D prostate mold is used as explained further below and ex-vivo MRI of the prostate specimen is performed as a high-resolution intermediate step to facilitate histology to in-vivo registration. Figure 1.1 shows the registration workflow used in this project. In a first step, in-vivo images are acquired in three orthogonal planes: para-axial, para-coronal and sagittal. The prostate is manually delineated from these images and then used for reconstructing the 3D prostate shape. This prostate shape is then subtracted from a software template of the mold. A

patient-specific mold is now obtained and is 3D-printed. After prostatectomy, the prostate is inked (to distinguish between left and right), the seminal vesicles are removed and the prostate is positioned in the mold. The prostate tissue is then fixated with formalin and imaged using ex-vivo MRI. After ex-vivo imaging, the prostate specimen is sliced using the cutting slots of the mold resulting in macroblocks, whose surfaces are identically oriented and positioned relative to the prostate as the in-vivo imaging planes. Thin slices are then sliced from the macroblocks and stained. These histology slices are examined under a microscope and imaged using a flatbed scanner [7]. In-plane 2D registration is finally done using in-house developed software.

The focus of the presented thesis within this project is on the processing of the ex-vivo imaging data. Since this is a completely untouched data set, the biggest challenge of the thesis is to identify and manage issues encountered in the ex-vivo workflow. Beyond this, the following result-oriented objectives are posed:

- To identify and quantify parameters from mp-MRI that can characterize tumor tissue, with focus on T2- and ADC-values
- To investigate the influence of the magnetic field strength of the scanner on the ex-vivo quantified parameters
- To investigate the influence of fixation time on the ex-vivo quantified parameters
- To correlate the ex-vivo quantified parameters with the corresponding in-vivo parameters and with the histological ground-truth

Whereas there is abundant literature about the correlation of mp-MRI with histological images, very little research can be found on the influence of the magnetic field strength and the fixation time on the ex-vivo quantification. Further, it is very interesting to examine the difference between the parametric values observed in-vivo and ex-vivo. To attain the goals listed above, a dedicated workflow for processing of the ex-vivo imaging data has been established in this thesis. It consists of data acquisition, registration and quantification and is explained in detail in the following chapters.

The thesis report starts with a literature overview to familiarize the reader with basic concepts and to review previous work in literature. Chapter 3 poses hypotheses about the expected results. Materials and methods are exposed in chapter 4 and the results of the investigations are given in chapter 5. The results are compared to the posed hypotheses in the discussion (chapter 6). Chapter 7 concludes the thesis.

Chapter 2

Literature review

First the general clinical context of prostate cancer is outlined. This provides the reader with a fundamental background on prostate cancer, its clinical handling and the margin for improvement. The clinical context is also necessary to be able to interpret the prostate images adequately. Secondly a detailed understanding of mp-MRI is gained. The different acquisition modalities and their clinical relevance are explained in depth. The third and final part handles about previous work done on the topic. Besides different methods for image registration, also results of correlating MRI-images with histology are reviewed. Additionally a subsection is dedicated to the patient-specific 3D mold.

2.1 Clinical context

2.1.1 Anatomy and function of the prostate

The left panel of figure 2.1 gives an illustration of the anatomical position of the prostate. It is located posterior (and superior) to the penis, inferior to the bladder and anterior to the rectum [11]. The base of the prostate is situated at the height of the bladder, while its apex ends in the urethral sphincter. The urethra runs straight through the prostate to transport urine from the bladder via the penis to the outside of the body. A capsule composed of collagen, elastin and large amounts of smooth muscle encloses the prostate gland. The prostate is supported anteriorly by the puboprostatic ligaments and inferiorly by the external urethral sphincter and perineal membrane. Its size and weight may vary with age, but on average it measures 3x4x2 cm and weighs 20 g [11].
Grossly, the prostate consist out of three zones (see right panel in figure 2.1): the central (CZ), transition (TZ) and peripheral zone (PZ). The PZ is the largest zone, comprising 70% of the volume and leaving 25% for the CZ and 5% for the TZ. It is also the zone where tumors are most occurring (70%) and it is palpated during digital rectal exam (DRE) (see next subsection). In addition to glandular tissue, the prostate also consists out of 30% fibromuscular stroma [11].

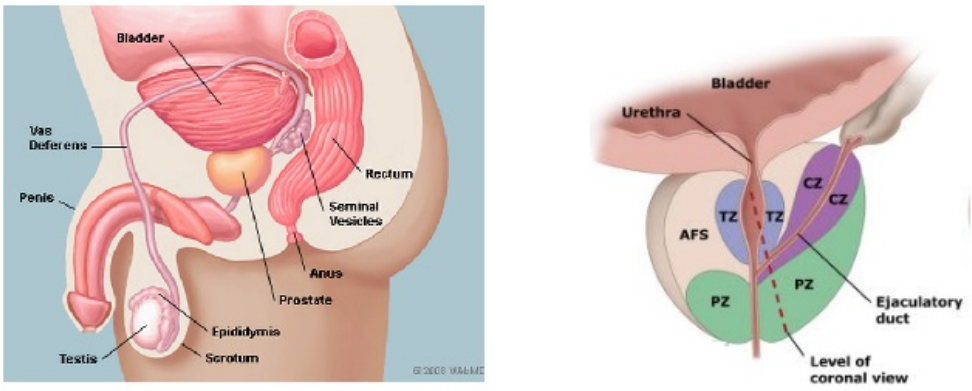

Figure 2.1: **Left**: anatomical position of the prostate (orange). **Right**: different zones of the prostate; CZ = central zone, TZ = transition zone, PZ = peripheral zone, AFS = anterior fibromuscular stroma [9][10].

The function of the prostate, being a male reproductive organ, is to secrete a fluid that is nutritive and protective for sperm. Additionally, it contains muscles that help to eject this fluid into the urethra during ejaculation. One of the components of the prostate fluid is the enzyme PSA. It has an important role in liquefying the semen, such that the sperm cells can move more fluently [12]. In a condition of benign prostatic hyperplasia or cancer, the prostate may be enlarged and may contain vast nodules. As a consequence, the urethra may be squeezed and urinating may feel sore [12].

2.1.2 Prostate cancer: symptoms and diagnosis

The most obvious symptoms of prostate cancer are nocturia, an increased frequency of urination and elevated levels of PSA [5]. However, these markers are not a definite conclusion towards cancer, since they might as well be present in benign prostate conditions. To come to a final diagnosis, the following methods are nowadays used: DRE, PSA-testing and transrectal ultrasound (TRUS) biopsy [5]. In DRE, the clinician reaches the prostate with one finger through the rectum. In this way the prostate gland is checked on enlargement and on the presence of tumors (may be felt as hard lumps) [13]. However, sensitivity of this method is limited because it enables only lateral and posterior investigation [5]. PSA-testing involves a simple blood test. If a man's blood contains between 4 and 10 ng/ml, this is suggestive for malignancy. A value higher than 10 ng/ml is highly suggestive for malignancy [5]. A final diagnostic decision is eventually made based on a TRUS biopsy. In TRUS biopsy, several regions of the prostate are sampled. A small plastic ultrasound transducer is inserted in the rectum together with a small needle. At different positions, the needle is fired to take tissue samples. These are then used for histopathologic examination and Gleason scoring. One drawback of TRUS is that possible sampling errors lead to

decreased sensitivity and specificity [5][14]. From the above, it is clear that mp-MRI may provide an improved way to detect and monitor prostate cancer.

2.1.3 Prostate cancer staging

Before a review is given of the present treatment methods for prostate cancer, it is important to have an idea about how the degree of cancer evolution is characterized. Indeed, this so called staging will eventually determine the choice of treatment. The most used tool to address the state of progression of (prostate) cancer is the TNM AJCC staging system (AJCC stands for American Joint Committee on Cancer) [15]. The staging system consists out of five elements, namely the tumor (T) category, the node (N) category, the metastasis (M) category, the PSA level and the Gleason score.

TNM categories

The T-category describes the size of the primary tumor and its penetration extent; e.g. T0 means that there is no evidence of a primary tumor. The N-category tells whether the cancer has spread to the nearby lymph nodes or not; e.g. N0 means that there is no spread to any nearby lymph node. Finally, the M-category assesses whether the cancer has metastasized to distant parts of the body or not; e.g. M0 means that no distant cancer spread was found. Furthermore, the T-category can be divided into the clinical T-stage (cT) and the pathological T-stage (pT). In cT-staging, the extent of the primary tumor is assessed in-vivo with techniques such as DRE, TRUS biopsy and medical imaging. pT-staging however, involves excision of the prostate and afterwards an ex-vivo histological examination. The latter assessment is to be considered more accurate and reliable [15]. Table 2.1 provides a detailed description of the TNM staging specific for prostate cancer.

PSA level

As already mentioned, PSA is an enzyme in the fluid secreted by the prostate. Its concentration in the body is measured with a simple blood test. Elevated levels of PSA may be caused by an enlarged prostate (aging), prostatitis and/or prostate cancer. An increased PSA concentration thus does not mean a definite conclusion towards prostate cancer. It rather is a sign for further investigation (e.g. DRE, TRUS biopsy ...). Values between 4 and 10 ng/ml are suggestive for malignancy. A value higher than 10 ng/ml is highly suggestive for malignancy [18].

Gleason score

The final element of the AJCC staging system includes the Gleason score. This measure indicates the aggressiveness of the tumor, which is related to the speed at which it is expected to grow. It is assessed based on histological examination after

Table 2.1: TNM staging system for prostate cancer [16].

T-stage	
cT	
cTX	Tumor cannot be measured
cT0	No evidence of a primary tumor
cT1	Clinically inapparent tumor not palpable or visible by imaging
cT2	Tumor confined within prostate
cT3	Tumor extends through the prostatic capsule
cT4	Tumor fixed or invades adjacent structures other than seminal vesicles (e.g. bladder, levator muscles, and/or pelvic wall)
pT	
pT2	Organ confined
pT3	Extraprostatic extension
pT4	Invasion of the bladder, rectum
N-stage	
NX	Regional lymph nodes were not assessed
N0	No regional lymph node metastasis
N1	Metastasis in regional lymph node(s)
M-stage	
M0	No distant metastasis
M1	Distant metastasis

needle biopsy or prostatectomy. The most abundant as well as the second most abundant type of tumor tissue receives a score out of five. The final score is the sum of both. The higher the score, i.e. the faster the tissue grows, the worse the prognosis. It should be noted that a biopsy involves small tissue samples. As a consequence, the assessed Gleason score may not be that accurate and may change after assessment based on prostatectomy [17]. Table 2.2 shows different values of Gleason scores with their accompanying clinical meaning.

Table 2.2: Gleason scores in ascending order and their meaning [16].

GX	Gleason score cannot be assessed.
Gleason < 6	The tumor is well differentiated and much likely to grow slowly.
Gleason 7	The tumor is moderately differentiated, moderately aggressive and likely to grow. However, it is not expected to spread quickly.
Gleason 8-10	The tumor is poorly differentiated, aggressive and likely to spread and grow rapidly.

Eventually, all the five elements of the TNM staging system are combined into a final stage assessment. The different groups are indicated as I - IV. A higher staging number means a more aggressive cancer, a worse prognosis and requires more

efficacious treatment methods. Table 2.3 indicates the characteristics of every stage group.

TABLE 2.3: Combination of the five elements of the TNM staging system to come to a final overall score (subdivisions are not shown) [16].

Stage	T	N	M	PSA [ng/ml]	Gleason
I	T1	N0	M0	< 10	< 6
IIA	T1	N0	M0	< 20	7
IIB	T2	N0	M0	any	any
III	T3	N0	M0	any	any
IV	T4	N0	M0	any	any

2.1.4 Treatment methods

Depending on the stage of the prostate cancer, different treatment methods may be applied. A list is given below, which in no manner is a complete overview of all the currently used methods.

Watchful waiting

In an early stage, the clinician may opt just to closely monitor the tumor development by DRE and to check PSA blood levels. Treatment is not immediately necessary because prostate cancer usually develops slowly. Also, the side effects of treatment may dominate the benefits [19]. The watchful waiting method is chosen when the cancer is not severe and thus not causing any cumbersome effects. It is often less preferably for younger men, since in the course of their life they will eventually experience problems due to the cancer and treatment will thus be needed after all [20].

Radical prostatectomy

The clinician may also suggest a radical prostatectomy. In this procedure the diseased prostate and often also the seminal vesicles are surgically removed. Depending on the N-stage of the TNM staging system, some of the lymph nodes may be removed as well. When many of the excised nodes contain malignant cells, prostatectomy may be interrupted because in that case the cancer is unlikely to be cured with surgery alone. Surgical techniques involve open and laparoscopic approaches. The open approach, in which one long incision is made (retropubical or perineal), may require prolonged healing. In the laparoscopic approach on the other hand, several small incisions are made and the prostate is removed using robotic tools. It often results in shorter stays in the hospital. Radical prostatectomy is mostly used for treating men with a moderately staged cancer that still have several years to live. Some side effects of the method include: bleeding, infections and damage to nearby organs [20].

Radiation therapy

In radiation therapy, high energy radiation or X-rays are fired at the malignant cells to kill them. Two types of radiation techniques exist: external beam radiation (EBR) and internal beam radiation (also known as brachytherapy). In EBR, the radiation is delivered from a machine external to the patient. It is mostly used for early-stage cancers. Prior to radiation, a simulation planning has to be done. This involves imaging of the prostate using computed tomography (CT) or MRI to assess the correct angles for the radiation beams and the proper dose. The therapy itself is painless. Newer variants of EBR are more tumor specific such that surrounding healthy tissue is preserved as most as possible. One of these techniques is intensity modulated radiation therapy. It involves a computer-driven machine, moving around the patient and constantly adjusting its beam angles and radiation intensity [20]. To be able to realize such a localized therapy, it is essential to localize cancerous regions on clinical images. One modality that can potentially meet this feature is mp-MRI. In brachytherapy, small radioactive units (e.g. iodine-125 or iridium-192) are placed into the tumor tissue. The malignant cells are then obliterated from the inside. This technique is also mostly used for early-stage cancers. However, a combination of brachytherapy and EBR can be effective in treating more aggressive conditions. When the prostate gland is too large, such that correct placing of the units becomes difficult, a hormonal pretreatment may be needed to shrink the prostate. Placement of the units is often guided by imaging techniques such as ultrasound, CT or MRI. Some side effects of radiation therapy include: irritation of the rectum, diarrhea, urinary incontinence and erection problems. The technique is used as an alternative for radical prostatectomy to treat early-stage cancers. It is also the designated method to fight recurrent tumors or to keep tumor development under control as long as possible [20].

Cryotherapy

Another treatment method for (prostate) cancer is cryotherapy. It applies very low temperatures in order to freeze malignant cells. TRUS is used to guide hollow probes through the skin into the prostate. Ice cold gases can in that way reach the prostate and kill the targeted cells. Warm saltwater is circulated through a catheter in the urethra during the procedure to keep it from freezing [20]. Since cryotherapy is not much invasive, it implies less blood loss and a shorter recovery period. However, about its long-term effects not so much is known. Side effects include blood in urine, erection problems and urinary incontinence. The technique is mostly used as an alternative for radiotherapy to treat recurrent cancers.

Hormone therapy

Hormone therapy is also termed androgen deprivation therapy (ADT). ADT aims to suppress the amount of male hormones (androgens) since they stimulate prostate cancer growth. It always has to be used in combination with one of the abovementioned methods in order to really cure the state of cancer. One method of hormone

therapy is orchiectomy, in which the testicles of the patient are removed. Since these are the main production side of male hormones, this removal drastically decreases androgen production. Another possibility is to administer drugs, for example luteinizing hormone-releasing hormone agonists, that impede the testicles to produce androgens. A few of the many side effects include: anemia, osteoporosis, weight gain, erection problems ... Hormone therapy is mostly used when surgery and radiation are ineffective or in combination with radiation to prevent the cancer from recurring [20].

Chemotherapy

When the cancer has spread, i.e. there is significant metastasis, the designated method to choose is chemotherapy. In this method, drugs are brought into the bloodstream which in this way are able to reach all the metastasized organs. Chemo is given in cycles, including rest periods, such that the patient's body is able to recover. The drugs involved in chemotherapy attack rapidly dividing cells. Besides cancer cells, also for example cells in the bone marrow and in the hair follicles are thus attacked. As a consequence, chemotherapy shows some typical side effects, including: hair loss, loss of appetite, nausea, vomiting and diarrhea [20].

Table 2.4 summarizes the functionality, selection and possible side effects of each treatment method.

2.2 Multiparametric MRI

MRI is an imaging technique based on the magnetic properties of protons. Proton spins are aligned by an external magnetic field and then disturbed by applying a radio-frequent (RF) pulse (90° or 180° flip angle). Returning to their equilibrium alignment, i.e. relaxation, the protons emit RF energy that is captured by coils. This captured signal is then transformed into image intensity information [21]. Two main types of relaxation exist: T1 - and T2-relaxation. The former happens through spin-lattice interactions, the latter through spin-spin interactions with surrounding molecules [23]. By varying repetition time (TR) and echo time (TE) different weightings for MRI-images can be achieved. For more details on the principles of MRI, the reader is referred to [23] p.64-104.

The multiparametric form of MRI, namely mp-MRI, has great potential to become the pre-eminent tool for detecting, monitoring and assessing the state of aggressiveness of prostate cancer. It consists of T2w-MRI, DWI, DCE-MRI and MRS. This set of different acquisitions provides fundamental quantitative information that is needed to quantify certain cancer characteristics. In what follows, every imaging modality is explained and also its relevance for quantifying prostate cancer is shortly touched upon. Additionally, localizer and T1-weighted imaging are included in the overview.

Table 2.4: Summary of different treatment methods for prostate cancer. The table highlights per method the functionality, arguments to choose a certain treatment and side effects.

Treatment method	**Functionality**	**Selection**	**Side effects**
Watchful waiting	Monitor tumor development by DRE and checking PSA blood levels	Cancer not severe and cumbersome. Mostly for elderly.	- tumor development not arrested
Radical prostatectomy	Prostate surgically removed	For moderately staged cancers	- bleeding - infections - organ damage
Radiation therapy	High energy radiation kills cancer cells	For early-stage and recurring tumors	- diarrhea - incontinence - erection problems
Cryotherapy	Malignant cells are freezed	To treat recurring cancers	- blood in urine - incontinence - erection problems
Hormone therapy	Supress amount of androgens	When surgery and radiotherapy fail or in combination with radiotherapy	- anemia - osteoporosis - weight gain - erection problems
Chemotherapy	Drugs brought into bloodstream	For metastasized cancers	- hair loss - loss of appetite - nausea/vomiting - diarrhea

2.2.1 Localizer imaging

Prior to acquiring an image sequence, a localizer scan is done to obtain distortion-free images. It images three orthogonal planes to assure that the endorectal coil is positioned correctly and to identify the relative anatomical position of the subsequently acquired images. Typically, a single-shot fast spin-echo (SSFSE) sequence is used for a localizer scan [22][24].

2.2.2 T1-weighted imaging

T1-weighted images have both a short TR and TE [23]. Since they particularly provide anatomical information, they are not a core part of mp-MRI. However, T1w-images show good contrast for hemorrhages, which will appear hyperintense. Oppositely, blood appears hypointense on T2w-images. So in the case that a hypointense spot is found on a T2w-image, the T1w-image can be used to check whether the spot is a bleeding or suggestive for cancer. A possible pulse sequence for T1w-imaging is a 2D gradient echo sequence [24].

2.2.3 T2-weighted imaging

T2-weighted images require both a long TR and TE [23]. They are often acquired with a fast spin-echo sequence. T2w-MRI is the fundamental component of mp-MRI since, besides high-resolution anatomical information, it provides quantitative information in the form of T2-maps. These maps display tissue-specific T2-relaxation times for every voxel [24]. The relevance of T2-maps for characterizing tumor tissue lies in the amount of free protons. Since cancerous tissue is more densely packed, it contains less free protons than healthy tissue. For stationary protons, the magnetic field inhomogeneity is relatively stable, resulting in strong spin-spin interactions and thus short T2-relaxation times in tumor tissue [23].

2.2.4 Diffusion-weighted imaging

Molecules are in constant Brownian motion due to thermal agitation. This motion or diffusion can be captured with DWI. It utilizes a pulsed gradient spin-echo (PGSE) sequence that emphasizes the dephasing caused by random thermal diffusion. This dephasing causes significant signal loss since each voxel contains a large number of molecules, each with a different motion. The measured signal $S(b)$ in isotropic media can then be written as an exponential:

$$S(b) = S_0 e^{-bD} \tag{2.1}$$

$$b = \gamma^2 \delta^2 (\Delta - \frac{\delta}{3}) G^2 \tag{2.2}$$

where S_0 is the unattenuated signal, b is the diffusion weighting and D is the diffusion coefficient [23]. In the formula for the diffusion weighting is γ the gyromagnetic ratio, δ the on-time of each of the gradients, Δ the time between the application of the two gradients and G is the magnetic field strength. When at least two signal measurements are done (one with b = 0 and one with b > 0), D can be calculated. Figure 2.2 illustrates the principle. Doing multiple measurements with multiple b-values increases the accuracy of D, but requires longer scan times and yields a decreased signal-to-noise ratio (SNR) [25]. In reality, random Brownian motion is not the only factor that contributes to the total diffusion coefficient. Also for example micro-circulation in the capillaries has an influence. Therefore, in practice the term apparent diffusion coefficient (ADC) is used, expressed in mm^2/s. When calculated for every voxel, an ADC-map is obtained [23].

DWI is the prominent modality to characterize tumor tissue. Indeed, cancer formation yields malignant cell proliferation and more densely packed tissue. Hence, diffusion will be more restricted and the ADC will decrease.

Extending DWI to anisotropic media yields diffusion tensor imaging (DTI). Since in anisotropic media diffusion is dependent on the direction, D now becomes a tensor

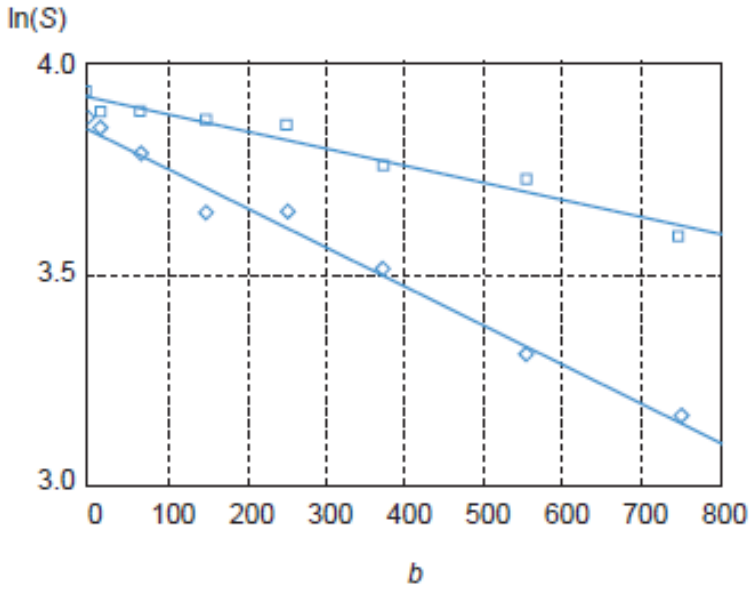

Figure 2.2: When multiple signal measurements are done for different b-values, the slope of ln(S) versus b yields the diffusion coefficient D. Adapted from [23].

(in casu a 3x3 symmetric matrix). D now has six degrees of freedom and thus measurements in at least six different noncollinear directions are needed on top of the blank measurement S_0. A popular way to express anisotropic diffusion is via its principal direction combined with the fractional anisotropy (FA):

$$FA = \frac{1}{\sqrt{2}} \frac{\sqrt{(\lambda_1 - \lambda_2)^2 + (\lambda_2 - \lambda_3)^2 + (\lambda_1 - \lambda_3)^2}}{\sqrt{\lambda_1^2 + \lambda_2^2 + \lambda_3^2}} \tag{2.3}$$

where λ_1, λ_2 and λ_3 are the principle eigenvalues of the tensor D [23].

2.2.5 Dynamic contrast-enhanced imaging

DCE-MRI delivers the possibility for imaging and quantification of tissue perfusion. T1-weighted acquisitions are done before, during and after rapid intravenous administration of a gadolinium-based contrast agent. Besides qualitative assessment, DCE-MRI-images can either be analyzed in a semi-quantitative or quantitative way. The former involves measures such as peak enhancement and rate of wash out (Rwo), the latter uses pharmacokinetic models and provides the transfer constant K_{trans} and the extracellular-extravascular compartment volume fraction V_e [25].
Compared to T2w-MRI and DWI, DCE-MRI is not a dominant component of mp-MRI since it does not have major discriminative power to distinguish the condition of cancer from other benign conditions. It is thus rather considered as an adjunct modality. DCE-MRI is however very useful in detecting recurrent tumors [25].

2.2.6 Magnetic resonance spectroscopy

The last imaging modality of mp-MRI is MRS and provides metabolic information about citrate, creatine and choline concentrations. Since these metabolites are much less abundant than water, water suppression sequences have to be used: for example a stimulated echo acquisition mode (STEAM) sequence [24]. Tumor tissue shows elevated choline and decreased citrate levels. MRS thus has great potential to increase prostate cancer detection rates. However, its clinical relevance stays limited because of the prolonged acquisition protocol and difficulty of accurate interpretation [25].

2.3 Previous work

2.3.1 Registration of in-vivo to histology images

In order to establish a parameter set from mp-MRI that correlates with tumor aggressiveness, in-vivo MRI-images need to be registered with the histological ground-truth. To this end, various methods have been described in literature. The registration procedure used in the current project is also discussed below.

Previous methods used in literature

Xu et al. [26] examined prostate tissue both in-vivo and ex-vivo. The histology slice plane was visually compared to the ex-vivo imaging planes and the best corresponding slices were selected. To account for histological slicing and mounting distortions, a 2D thin plate spline warping was performed. Further, ex-vivo parametric images were transformed into the in-vivo coordinate system based on manual alignment of intra-glandular structures. Finally, they used an unsupervised 3D affine transformation to register in-vivo parametric images to the in-vivo space. As can be noticed, this registration procedure is computationally intensive and cumbersome. It also involves a lot of manual labor and may thus be rather subjective.
Uribe et al. [27] inserted a plastic rod through the urethra to facilitate MRI to histology registration. The rod appeared hypointense in the images and that allowed to select a corresponding histology slice with approximately the same orientation. Ex-vivo and in-vivo to histology registration was done using the Elastix software [28]. An initial affine transformation provided a first rough alignment of the images. A second non-rigid b-spline transformation was subsequently applied to account for possible deformation. Although the use of the plastic rod may provide more accurate results, the method for selecting corresponding slices stays rather heuristic.
A first kind of mold is used by Reynolds et al. [29]. They fixated prostates with formalin and mounted them in agarose gel in a custom designed box. Ex-vivo to in-vivo registration was done by a cubic-spline based non-rigid registration. Since the box provided matching slices, ex-vivo to histology registration could be done by a rigid registration. However, since the mold was not patient-specific, still a 3D transformation was needed to align the in-vivo and ex-vivo data.
Finally, Priester et al. [30] report the use of a patient-specific 3D-printed mold for

MRI to histology registration. The prostate contours were manually delineated on in-vivo images, from which the mold was constructed. The mold had evenly spaced parallel slits, each of which corresponding to a known in-vivo slice. The prostate was sliced and every histology slice was delineated by a pathologist. These lesion contours were then elastically warped to fit the in-vivo contours. The method described here, however does not use ex-vivo images as an intermediate step to register in-vivo to histology images.

Method used in the present project

As already mentioned in the introduction, the present project uses ex-vivo images as an intermediate step to facilitate in-vivo to histology registration. Since these ex-vivo images are of much higher resolution than their in-vivo counterparts, they enable a more accurate registration. Furthermore, a patient-specific mold is used to facilitate ex-vivo to in-vivo registration. For the different steps of the registration procedure, refer to figure 1.1. In this section, more attention is paid to the advantages and features of the patient-specific mold.

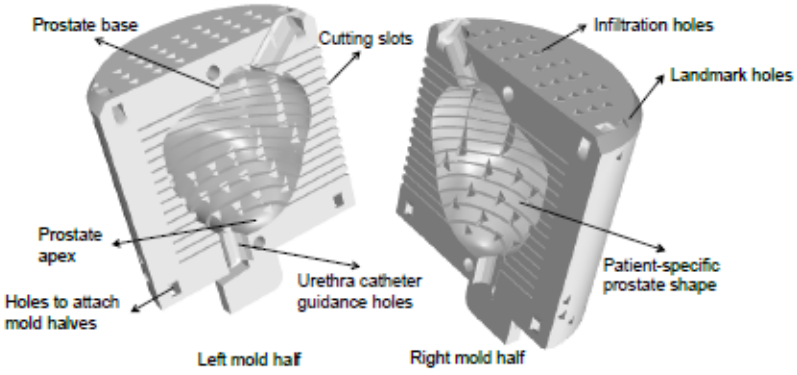

Figure 2.3: Patient-specific prostate mold design for registration of histology to in-vivo and ex-vivo MRI with indication of its main features. Adapted from [7].

Figure 2.3 depicts the design of the mold. It consists of two halves (left and right or front and back) that enclose the exact shape of the patient-specific prostate. Further, the mold has parallel cutting slots that are equally spaced on a distance determined from in-vivo delineations (in casu 3 mm). The cutting slots have the same orientation and position relative to the prostate as the corresponding MRI slices. This reduces the registration problem from 3D to 2D [7]. This assumption is only valid however when the excised prostate is positioned precisely in the mold. To assure this, the mold has some specific features. The start and end points of the urethra are specified as additional landmarks at the surface of the prostate. They are used as guides for a catheter that is inserted into the urethra to constrain the positioning of the prostate in the mold. It reduces out-of-plane rotational offsets [7]. Additionally,

the mold design shows parallel channels orthogonal to the cutting slots. They allow an external fixation medium (e.g. formalin) to reach the interior tissue such that the prostate can be fixated while in the mold. In that way, rigidity problems due to prior fixation are avoided and the tissue is fixated corresponding to its in-vivo shape thus providing an optimal positioning in the mold. The design allows ex-vivo images to be acquired with the same orientation and position as the in-vivo images. Consequently, they can be used swiftly as high-resolution intermediates to facilitate histology to in-vivo registration.

The registration itself proceeds in two steps. Assuming a good fit and correct positioning of the ex-vivo prostate in the mold, the ex-vivo to in-vivo registration can be done with a simple rigid transformation. The mold can be directly overlaid with the in-vivo images, since it was created from in-vivo delineations. This simplifies the registration to a rigid alignment of the mold. To align the histology and ex-vivo images, a b-spline non-rigid registration is performed on each slice, based on corresponding high-resolution tissue features. A non-rigid registration is needed here because the histology images may deform during the slicing process. Histology to in-vivo registration is then realized by combining both (rigid and non-rigid) transformations [7].

2.3.2 Correlation of mp-MRI with histology

Abundant literature is available about the correlation between parameters of mp-MRI and an histological ground-truth. Although the present project focuses on DWI and T2w-MRI, a complete overview is given here, thus also considering parameters from DCE-MRI and MRS. In general, there is a consensus that T2-values as well as ADC-values decrease in tumor tissue compared to healthy tissue (also refer to table 2.5).

Jacobs et al. [5] did a literature overview, investigating the relevance of parameters of DWI, T2w-MRI and MRS. They report that healthy prostatic tissue shows higher T2-values than tumor tissue. Some tumors in the TZ however show the same T2 signal characteristics compared to a condition of benign prostate hypertrophy. This reduces the sensitivity of using T2w-MRI alone. Further, they report a reduction of 20% - 40% in ADC-values in cancerous tissue compared to healthy tissue. Including DWI highly increases the sensitivity and specificity for tumor detection. Also, there are regional variations [5]: 'in the PZ ADC-values are greater (1.5-2.0 $10^{-3}mm^2/s$) than the ADC-values in the CZ (1.4-1.7 $10^{-3}mm^2/s$)'. Concerning MRS, they mention an increased choline and a decreased citrate concentration to be potential markers for malignancy.
These conclusions are further supported by Groenendaal and colleagues [31]. They constructed a statistical model for voxel classification to delineate prostate tumors. Highly suspicious voxels were identified based on low T2-values, low ADC-values and high K_{trans}-values (obtained from DCE-MRI). Other parameters obtained from DCE-MRI are investigated by Singanamalli et al. [32]. Their paper correlates ex-vivo

microvessel features from histological slices with in-vivo DCE-MRI kinetic parameters, namely the Rwo and initial area under the curve (IAUC). The results pointed out that benign tissue shows a more uniform distribution of microvessels, whereas tumor tissue consists of a heterogeneous microvessel arrangement. This difference can partly be captured by looking at the Rwo and IAUC. However, the density of angiogenesis is influenced by a lot of other factors, for example genetic factors. Therefore the use of DCE-MRI to characterize tumor tissue is more ambiguous. This is moreover confirmed by Isebaert and colleagues [33], who used generalized estimating equations to estimate the sensitivity, specificity, accuracy, positive and negative predictive value for T2w-MRI, DWI and DCE-MRI. Results show that DWI has the highest sensitivity for tumor localization (44.5%) followed by T2w-MRI (31.1%) and concluded by DCE-MRI (27.4%).

It is also interesting to see how in-vivo parameters compare to ex-vivo parameters. Xu et al. [26] for example examined the diffusion characteristics (DWI and DTI) of histologically defined prostate cancers in-vivo and ex-vivo. They found a 50% reduction in ADC-values in cancerous tissue compared to healthy tissue. Also, a 50% reduction in ADC-values was found ex-vivo compared to in-vivo. For the DTI, no significant differences were found in FA-values when comparing cancerous and benign tissue in the PZ. However, DTI may provide a unique contrast that is able to differentiate prostate cancer in the CZ.
A similar study was conducted by Uribe et al. [27]: their purpose was to investigate whether the FA (in-vivo as well as ex-vivo) can contribute on top of the ADC to the grading of prostate cancer. Confirming Xu et al., they report a reduction in ADC-values of about 50% ex-vivo versus in-vivo. Depending on the stage of the cancer, a reduction of approximately 32% was found in malignant tissue relative to benign tissue. Similar observations can be made when comparing T2-values ex-vivo versus in-vivo [34][35]. The FA-values were significantly higher in tumor tissue, however only in-vivo. Uribe et al. explain that this increase in FA-values is caused by the lower SNR of the in-vivo images, rather than by the presence of cancer. They consequently conclude that FA does not significantly contribute to the grading of prostate cancer.

Bourne et al. [39] observe a multi-exponential signal decay (mESD) when performing DWI over an extended range of b-values. Compared to the conventionally assumed mono-exponential model, mESD analysis may provide higher specificity for detection of cancer. The origin of mESD in biological tissues is assumed to lie in the existence of biologically distinct microenvironments with each their own characteristic diffusion properties. The observed decrease in ADC-values in-vivo in a condition of prostate cancer is expected to result from an increase of partial volume of epithelial tissue and simultaneous decrease of stromal tissue and ductal space [40].

To conclude this subsection, table 2.5 summarizes typical T2- and ADC-values observed in literature. This table may be used later on to benchmark obtained results. Values are grouped according to the tumor zone and whether they were observed

in-vivo or ex-vivo. As can be noticed, papers that quantify ex-vivo T2-values are scarce in literature. Further, most values apply to the PZ. This is logical since the PZ comprises the majority of prostate tumors. On average for the PZ, T2-values decrease 20% in tumor versus healthy tissue and 47% ex-vivo versus in-vivo. ADC-values show a corresponding 35% and 47% average decrease. Ex-vivo values are lower than in-vivo values due to formalin fixation (see subsection 2.3.4).

TABLE 2.5: Typical T2-values and ADC-values found in literature: summary of eight papers. A comparison is made between values for healthy (subscript 'he') and tumor (subscript 'tum') tissue.

Protocol	**Reference**	$\mathbf{T2_{he}}$ $[ms]$	$\mathbf{T2_{tum}}$ $[ms]$	$\mathbf{ADC_{he}}$ $[10^{-3}mm^2/s]$	$\mathbf{ADC_{tum}}$ $[10^{-3}mm^2/s]$
PZ in-vivo	Uribe [27]				1.41 ± 0.20
	Jacobs [41]			1.61 ± 0.26	0.83 ± 0.17
	Foltz [35]	104 ± 20	81 ± 7		
	Xu [26]			1.66 ± 0.21	0.94 ± 0.14
	Liu [36]	149 ± 32	100 ± 10		
	Roebuck [37]	193 ± 49	100 ± 26		
	Metzger [38]	128	96	1.38	0.86
PZ ex-vivo	Glorieux [34]	53 ± 28	48 ± 24	0.54 ± 0.13	0.50 ± 0.09
	Uribe [27]				0.74 ± 0.09
	Jacobs [41]			0.72 ± 0.11	0.54 ± 0.12
	Xu [26]			0.84 ± 0.13	0.43 ± 0.06
CZ in-vivo	Jacobs [41]			1.59 ± 0.22	1.01 ± 0.15
	Foltz [35]	76 ± 7	81 ± 7		
TZ ex-vivo	Glorieux [34]	53 ± 20	51 ± 18	0.61 ± 0.15	0.45 ± 0.12

2.3.3 Influence of magnetic field strength of scanner

Much less literature is available about the influence of the magnetic field strength of the scanner on the quantified parameters, certainly ex-vivo. Until now, all the work has been limited to in-vivo studies and information about a potential influence on T2- and ADC-values is very scarce.

A first study compares two in-vivo 3T scanners, one from General Electric (MR 750, Milwaukee, MI, USA) and one from Philips (Achieva Xseries, Best, The Netherlands), for prediction of in-vivo T2-values. Conform with the previous subsection, they found lower T2-values in malignant tissue compared to healthy tissue. However, there was no significant difference in mean T2-values on both scanners [42].
Bratan et al. [43] investigated the influence of imaging and histological parameters on prostate cancer detection rates. In-vivo MRI was performed on a 1.5T and 3T scanner. Cancer detections were done visually and independently by two radiologists based on focal abnormalities. Later, these findings were tested against whole-mount

histological slices. The conclusion was that detection rates were influenced by tumor characteristics such as Gleason score, volume, location ..., but neither by field strength nor coils used for imaging.
Another study by Mazaheri and colleagues [44] examined the presence and extent of artifacts in prostate DWI produced by a 1.5T or 3T scanner. Again, this involved an in-vivo study and ADC-maps were not included in the analysis. In conclusion they report that scanning at 3T yields a better SNR at the expense of increased geometric distortion. Scanning at higher field strength may also lead to more pronounced ghosting artifacts.
In the same article it is mentioned that Rosenkrantz et al. [45] compared DWI of abdominal organs in terms of image quality and ADC-values obtained at 1.5T and 3T. Similar ADC-values were found on both scanner types for all assessed organs.

2.3.4 Influence of fixation time

Also interesting to know is whether the fixation time has an influence on obtained ex-vivo quantified parameters. For example when a sample is scanned a second time because the first scan was not satisfactory, the observed parameters may have changed during the elapsed time between the two scans due to a longer fixation time. Articles that explicitly handle this topic are again scarce. However, Bourne et al. [46] performed a study that is very useful to address this problem. They evaluated the effect of formalin fixation on bi-exponential modeling of diffusion decay in prostate tissue. Three excised prostate specimens were imaged before and after fixation. The results showed a significant reduction in mean ADC due to fixation. This can be extended to T2-values, which also decrease with fixation. The fixation process is expected to induce a change in tissue architecture and thus diffusivity. Also, it reduces the amount of free protons, leading to a stable magnetic field inhomogeneity and thus shorter T2-values. Acknowledging this effect, it can be expected that T2- and ADC-values will be lower when fixated for a longer time, thus when quantified at a later time point of scanning.
Furthermore this effect explains why ex-vivo parametric values are lower than the in-vivo equivalents. When excised (thus ex-vivo), a prostate specimen is fixated and preserved using formalin. This fixation reduces T2- and ADC-values as explained.

Chapter 3

Hypotheses

Based on the literature study and rationale, the following hypotheses are posed:

- T2- and ADC-values will decrease both in-vivo and ex-vivo in tumor tissue compared to healthy tissue
- T2- and ADC-values will decrease ex-vivo compared to in-vivo
- T2- and ADC-values will be lower for longer fixation times
- T2- and ADC-values will not be influenced by the magnetic field strength of the scanner

The first hypothesis should be clear from the literature study. As already mentioned, tumor tissue consists out of a large amount of densely packed cells. Hence, it contains less free protons and diffusion will be restricted. Consequently, T2- and ADC-values will decrease in tumor compared to healthy tissue. This has already been confirmed in literature. Also the second hypothesis has been abundantly observed in literature. The reasoning why ex-vivo values will be lower than in-vivo values is already given in section 2.3.4.
The same explanation, i.e. formalin fixation, can be invoked to justify the third hypothesis. However, only few articles have investigated this issue.
Finally, the last hypothesis is the most uncertain since no relevant work can be found in literature. It is based on the following argumentation. The main difference between the two ex-vivo scanners available in this thesis is their magnetic field strength: 7T versus 9.4T. T2-weighting depends on the relative TR and TE, but not on the field strength. Therefore T2-values are expected to be similar on both scanner types. Equation 2.2 shows that DWI does depend on the field strength. It further indicates that with the 9.4T scanner higher b-values can be attained. This means that there will be a difference in fitting (refer to figure 2.2): the 9.4T scanner allows to fit a wider range of b-values. The fit thus may be more accurate on the 9.4T scanner, but will be similar compared to the 7T scanner. The signal strength furthermore drops exponentially with the b-value, so data points at higher b are less determinative. The hypothesis is thus that T2- and ADC-values will be similar on both scanner types.

Chapter 4

Materials and methods

This chapter describes in detail the complete workflow of the current project. Figure 4.1 provides an overview. The pink shaded boxes on the left hand side describe the prior workflow, including all the steps aside from ex-vivo image processing. The focus of this thesis however is on the ex-vivo workflow, which consists out of three main parts: data acquisition, registration and quantification. Results from the quantification may be fed back to the data acquisition part to adapt for example the ex-vivo imaging protocol to achieve more satisfying outputs. The remainder of this chapter elaborates every step of the project workflow in depth.

4.1 Prior workflow

4.1.1 Patient recruiting

Nineteen patients were recruited for this project starting from December 2016 until April 2018. They all had biopsy proven prostate carcinoma with an average Gleason score of seven. Informed consent was obtained from each patient before inclusion into the study and the prostates were imaged both in-vivo and ex-vivo (after excision). Patients for which the prostate did not fit into the mold (see subsection 4.1.4) were excluded. Due to scanner defects or errors in the ex-vivo image acquisition protocol, no usable ex-vivo scans could be acquired for four of the nineteen patients. This left a total of fifteen subjects included in the study.

4.1.2 In-vivo imaging

In-vivo imaging was performed on a 1.5T device (Siemens MAGNETOM Aera syngo MR D13, Erlangen, Germany). T2w-scans were acquired in three orthogonal planes: axial, coronal and sagittal using a turbo rapid imaging with refocused echoes (RARE) sequence. These could be used later on to reconstruct the 3D prostate shape. Additionally, axial diffusion scans were obtained with a spin-echo (SE) protocol with a total of six b-values. Table 4.1 shows the most important imaging parameters for each

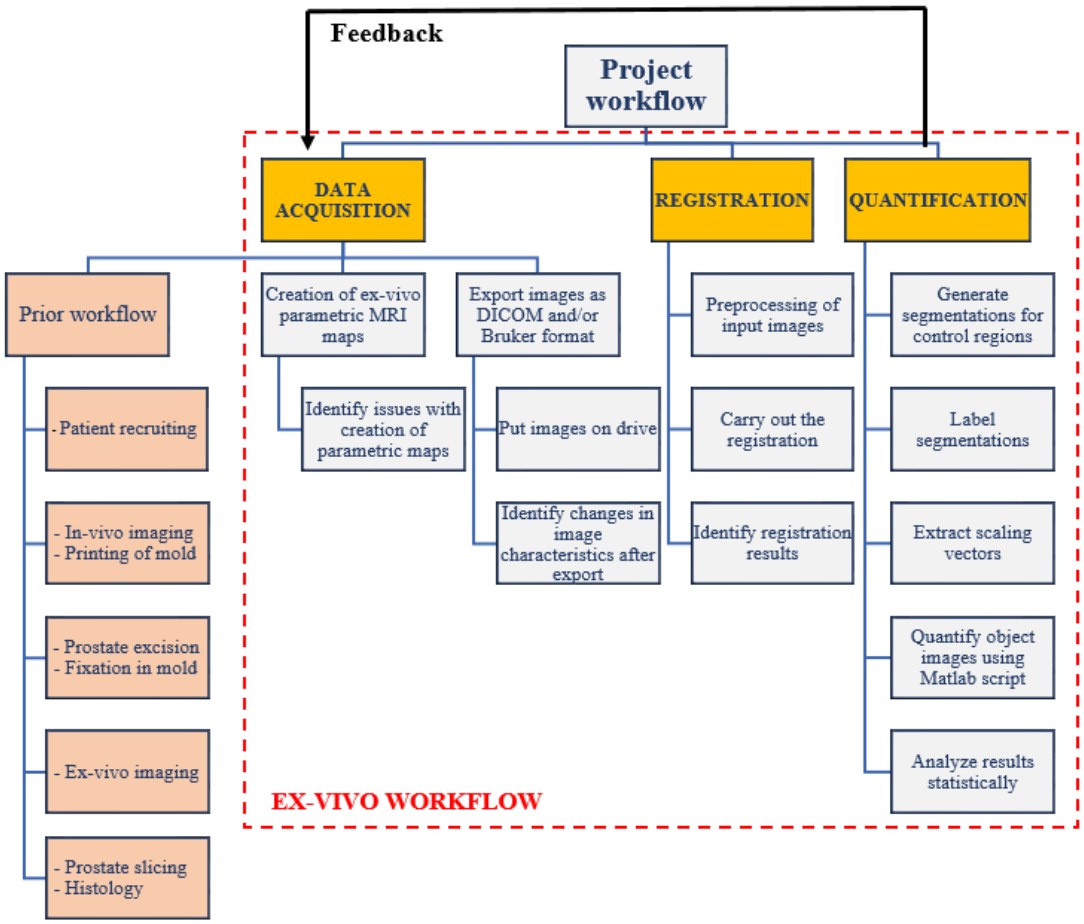

Figure 4.1: Overview of the complete workflow describing the current project. The ex-vivo workflow - on which this thesis is focused - is indicated with a red dotted box. The other part of the workflow (prior workflow) is not the core business of this thesis but is important for the complete project.

scan type. For subject 15 however, in-vivo imaging was carried out externally and the parameters differed. The T2w-scans had a matrix size of 320 x 320 pixels, voxel size of 0.688 mm x 0.688 mm and slice thickness of 4 mm. The diffusion scan had a matrix size of 112 x 112 pixels, voxel size of 1.786 mm x 1.786 mm and slice thickness of 4 mm.

4.1.3 Printing of the mold

As mentioned before, in-vivo T2w-images were acquired in three orthogonal planes: axial, coronal and sagittal. The prostate was then manually delineated on the T2w-scans. These in-plane delineations were used to reconstruct the 3D prostate shape, which was subsequently subtracted from a software mold template. The

TABLE 4.1: Summary of the most important in-vivo imaging parameters for each scan type [48].

Scan	**Matrix size**	**Voxel size** $[mm]$	**Slice thickness** $[mm]$	**TR** $[ms]$	**TE** $[ms]$	**Flip angle** $[°]$
T2_Turbo RARE_axial	406 x 448	0.580 x 0.580	3	11250	124	160
T2_Turbo RARE_sagittal	448 x 448	0.580 x 0.580	3.5	7700	133	160
T2_Turbo RARE_coronal	448 x 448	0.580 x 0.580	3.5	14010	124	160
SE_DWI_axial	104 x 128	2.734 x 2.734	4	9900	67	90

mold had a cylindrical shape with a diameter of 6.4 cm and length of 6 cm [34]. The patient-specific mold was then 3D-printed on a UP! Plus 2 3D-printer (PP3DP UP!, noDNA GmbH, Berlin, Germany) using acrylonitrile butadiene styrene. The complete process of printing both mold halves took about 24 hours and the result was delivered with a resolution of 150-400 μm [34].

4.1.4 Prostate excision and positioning in the mold

Surgical resection of the prostate was done by robot assisted laparoscopic prostatectomy, a minimally-invasive procedure in which the prostate was reached via incisions in the lower abdomen (see subsection 2.1.4). Through each incision, not larger than 1 cm, thin tubes were placed. A small camera was guided through one of the tubes to visualize the process, while carbon dioxide was injected into another to expand the surgical area. Through the other tubes, the surgical instruments were operated. More specifically, the instruments were operated very precisely via a robotic console [49]. After excision, the prostate was positioned as accurately as possible in the mold using the dedicated features described in section 2.3.1. Also, the specimen was fixated with formalin. Sometimes it occurred that the excised prostate was too big to fit in the mold. This was often due to an erroneous estimation of the specimen's volume based on the in-vivo images caused by the presence of fluid surrounding the prostate. Unfortunately, the sample could in this case not be used for the study.

4.1.5 Ex-vivo imaging

For ex-vivo imaging, two scanning devices with different magnetic field strengths were available: a 7T and a 9.4T Biospec MR scanner (Bruker Biospin, Ettlingen, Germany). Both had a bore of 200 mm diameter and a gradient amplitude of 200 mT/m and 600 mT/m respectively [50]. Acquisition was performed using vendor's software called Paravision. Whereas acquisition on the 7T scanner was performed

using Paravision 6, the 9.4T used either Paravision version 5 or 6 (but mostly version 5). Both software versions merely differed in terms of user interface: images acquired in Paravision 5 or 6 had completely equal characteristics. Whether imaging was done on the 7T or 9.4T scanner depended on their availability. Some specimens were scanned on both devices to be able to investigate the influence of the magnetic field strength on quantification. Table 4.2 summarizes for both scanners the different types of scans conducted and their most important imaging parameters. First, a localizer scan was done to check whether the ex-vivo mold position corresponded to the in-vivo imaging position. Next, a turbo RARE sequence was used to acquire T2w-scans and a fast low angle shot (FLASH) sequence to obtain 3D-images [51][52]. Furthermore, diffusion images (DWI and DTI) with varying number of directions and b-values were acquired using SE sequences. Since the 7T scanner was implemented with user-defined diffusion protocols, the number of directions and b-values could vary strongly per patient. Finally, also a T2-map was constructed using multiple echo time measurements. When the scanners were defect or when there were errors in the ex-vivo imaging protocol, none or only non-usable images were obtained. Patients for which this was the case, could not be included in the study.
As can be noted from table 4.2, the diffusion-weighted acquisitions on the 9.4T scanner had a fairly low resolution. This was unexpected since all the ex-vivo scans were supposed to be of high resolution. The reason for this low resolution was lack of time. DWI using multiple b-values and in particular directions, required a lot of scan time. In order to fit the scans within the twelve hour scan slot, the resolution had to be reduced. On the other hand, the 7T scanner did not allow very high b-values given its lower gradient amplitude. Instead, more time could be invested in a higher resolution.

4.1.6 Prostate slicing and histology

Prior to histology, the specimen was first inked to be able to distinguish between left (black) and right (blue). Afterwards, the prostate was sliced with a microtome using the prescribed cutting slots in the mold, thus producing slices of 3 mm thickness. The total number of slices depended on the size of the prostate. The slices were then placed on a glass plate in a specific pattern such that apex and base could be easily recognized. The front side as well as the back side were scanned with a flatbed scanner. The slices, also called macroblocks, were next passed to the histology section where very thin slices (5 μm) were taken from the macroblocks. These histological slices were then haematoxylin and eosin stained and examined by a pathologist: they constituted the ground-truth for tumor definition [34]. Since the thin slices might have been deformed during the cutting process, a non-rigid transformation was needed to register the histological slices to the in-vivo and ex-vivo MRI-images (see section 4.3).

TABLE 4.2: Summary of the most important ex-vivo imaging parameters used on the 9.4T and 7T scanner for each scan type.

9.4T scanner	**Matrix size**	**Voxel size** [mm]	**Slice thickness** [mm]	**TR** [ms]	**TE** [ms]	**Flip angle** [°]	**B-values** [s/mm^2]
Localizer multi 8cm	128 x 128	0.625 x 0.625	1	350	5	30	
T2_Turbo RARE	256 x 256	0.273 x 0.273	3	4500	37.64	90/180	
FLASH_3D	360 x 360	0.181 x 0.181	0.181	150	12	20	
SE_DWI 3dir_12bval	32 x 32	2.188 x 2.188	3	3600	29	90	[50, 219, 520, 961, 1546, 2281, 3169, 4212, 5415, 6779, 8307, 10000]
SE_DTI 6dir_1bval	64 x 64	1.094 x 1.094	3	3600	29	90	[1500]
SE_DTI 6dir_3bval	64 x 64	1.094 x 1.094	3	3600	29	90	[500, 750, 1000]
T2-map	256 x 256	0.273 x 0.273	3	4177	10	90/180	

7T scanner	**Matrix size**	**Voxel size** [mm]	**Slice thickness** [mm]	**TR** [ms]	**TE** [ms]	**Flip angle** [°]	**B-values** [s/mm^2]
Localizer multi 8cm	256 x 256	0.313 x 0.313	1	7	2.4	8	
T2_Turbo RARE	256 x 256	0.273 x 0.273	3	4500	37.5	90	
FLASH_3D	360 x 360	0.181 x 0.181	0.181	150	12/15	20/30	
SE_DWI 3dir_6bval	128 x 128	0.547 x 0.547	3	3600	30	90	[0, 200, 500, 900, 1250, 2000]
SE_DWI 3dir_8bval	128 x 128	0.547 x 0.547	3	3600	33	90	[0, 50, 250, 500, 1000, 1500, 2500, 3700]
SE_DTI 5dir_6bval	256 x 256	0.273 x 0.273	3	3600	31	90	[0, 150, 250 500, 1250, 2000]
SE_DWI 1dir_15bval	256 x 256	0.273 x 0.273	3	3600	31	90	[0, 50 ... 300, 400, 500, 750, 1000 ... 2000]
SE_DTI 6dir_4bval	256 x 256	0.273 x 0.273	3	3600	31	90	[0, 250, 500 1000]
T2-map	256 x 256	0.273 x 0.273	3	4500	10	90	

4.2 Ex-vivo workflow: data acquisition

4.2.1 Creation of ex-vivo parametric maps

After ex-vivo imaging, the raw diffusion- and T2-weighted acquisitions had to be converted into parametric maps using the Paravision software. As illustrated in figure 2.2, multiple measurements with different b-values (or different echo times for T2-map acquisitions) were needed to construct the maps. Simple built-in mono-exponential decay fitting functions were used:

$$S(b) = A + S_0 e^{-bD} \tag{4.1}$$

$$S(t) = A + S_0 e^{-\frac{t}{T2}} \tag{4.2}$$

with S, S_0, b and D as defined in equation 2.2, A the absolute bias, t the time and $T2$ the T2-relaxation time [53]. The software outputted one image stack, containing for each slice five parameter images or object types: the signal intensity image (S_0), the parametric map and the standard deviation images of the signal intensity image, the parametric map and of the whole fit. Figure 4.2 illustrates this with an example. When acquisition was not done according to protocol and no multiple measurements were obtained, creation of parametric maps was impossible. For the fifteen subjects included in the ex-vivo study however all the parametric maps could be constructed. Also, for some patients diffusion- and T2-weighted acquisitions were repeated to evaluate the impact of tissue fixation on ADC- and T2-quantification (see subsection 2.3.4).

4.2.2 Export of ex-vivo images

Ex-vivo imaging happened at the molecular small animal imaging centre (MoSAIC) in Leuven. From there, the images had to be exported to a secured on-line drive such that they were accessible from outside MoSAIC. Transfer to the drive had to be done by local admins, having write access. The images were exported as DICOM (digital imaging and communications in medicine) and as Bruker format.
The Bruker format could be converted to the Analyze format using a previously in-house developed conversion tool [54][56]. However, as explained below, the DICOM format was used in this thesis. DICOM is the international standard for processing medical images and it stores images with a separate file for each slice. Analyze is a less common format which has one file to store the actual data and a second file containing the header information [55][56].
After export, some of the image characteristics changed. Analyze images were flipped top-down, time points and object types were interchanged and the intensity values were scaled. DICOM images however only showed scaling of intensity values (but with a different scaling factor). This fact, namely that the DICOM standard was much more consistent in keeping its characteristics, was the main reason to work

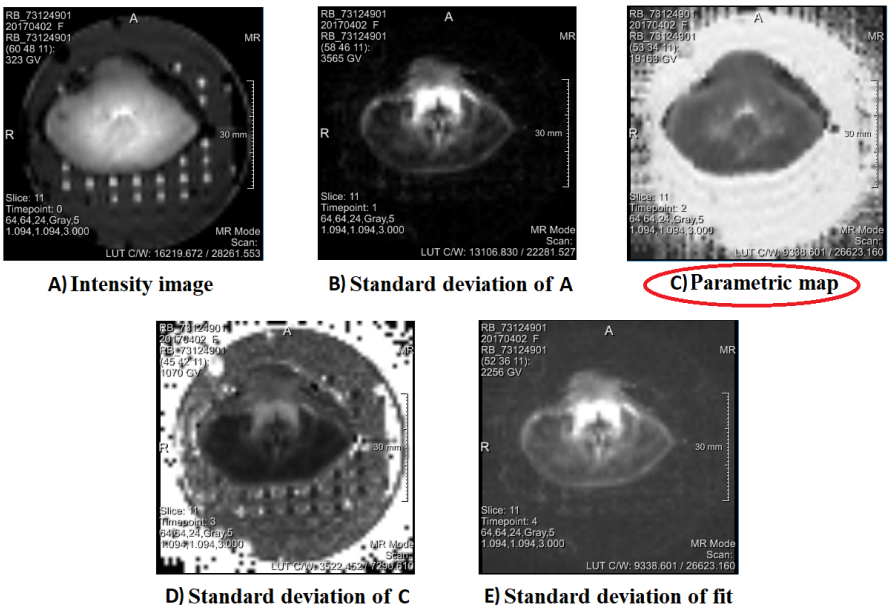

FIGURE 4.2: Besides the parametric map **(C)**, the Paravision software outputted in the same image stack for each slice the signal intensity image **(A)**, its standard deviation **(B)**, the standard deviation of the parametric map **(D)** and the standard deviation of the fit **(E)**.

with DICOM instead of Analyze in this thesis. The exported images were compared against the source images at MoSAIC to identify the scaling factors. Whereas the raw images had a constant scale factor that was identical for all slices in the scan, the parametric maps had slice-specific factors. Every scale factor could be retrieved from the individual DICOM headers. Correction for the scaling was done in the quantization procedure, thus after the registration. The main reason for this was that native ADC-values were very small (cf. table 2.5) and consequently the majority of the values would be read as zero in the registration tool, as this tool - implemented in the MeVislab software (MeVis, Bremen, Germany) - had a precision of only four decimals. Additionally, correction before registration was cumbersome due to conversion issues. Using Matlab (MathWorks, Natick, MA), it was possible to import and save images in TIFF (tagged image file format) format, but this changed the image characteristics [57]. Section 4.4 explains how the scaling issue was handled after registration.

4.3 Ex-vivo workflow: registration

Image registration is the process of transforming different images into a common coordinate system such that anatomically corresponding positions coincide. In this thesis, in-house developed software was used for 2D registration. This tool was

created in a previous project (DrTherapat) and was an interface module implemented in MeVisLab [7][58]. Until now, the tool is still being updated and small issues are regularly resolved.

4.3.1 Preprocessing of input images

Below, all the necessary inputs that needed to be specified in the data tab of the DrTherapat tool are specified. The inputs that are not directly clear from their name, are firstly further explained. The *left/right mold* and *back/front mold* were the stl-files (surface tessellation language) of the right and left or back and front mold as they were send to the 3D-printer. The *segmentations* input contained the final cso-file (contour segmentation objects) of the segmentations used to design the mold. *Nb plates* was the number of glass plates needed to scan the macroblocks. When all the inputs were specified once for a patient, they could be saved in a data file such that they could be reused in the future.

- Ex-vivo T2 2D
- Ex-vivo T2 3D
- Ex-vivo ADC
- In-vivo axial T2
- In-vivo coronal T2
- In-vivo sagittal T2
- In-vivo ADC
- Left/right mold
- Back/front mold
- Most apical histology slice
- Segmentations
- Nb plates

To be able to execute the registration properly, some inputs required preparation, namely the ex-vivo T2w 2D- and 3D-images, ex-vivo parametric maps and in-vivo ADC-maps. All these preprocessing steps were performed manually in MeVisLab. As already mentioned, DICOM images are stored with individual files for each slice. The first thing that had to be done for all images was thus to convert the separate files into stacks, i.e. 3D volumes. Then, for the ex-vivo T2w 2D-images and parametric maps the x- and y-axis had to be flipped to give them the same orientation as the in-vivo images. Additionally for the calculated parametric maps, the third object type had to be extracted to obtain the actual T2- or ADC-maps (see subsection 4.2.1). Finally, the interslice distance had to be checked and adapted if necessary to 3 mm for the ex-vivo T2w-images. The same conversion to 3 mm had to be done for the in-vivo ADC-maps, which were imaged at an interslice distance of 4 mm.

4.3.2 Registration

To register the in-vivo images with the histology slices, the DrTherapat tool had two registration pathways: one via the macroblocks and one via the ex-vivo images. In this project only the ex-vivo pathway was used since it leaded to more accurate results, given the high resolution of the ex-vivo images and possible deformation of the macroblocks during slicing. Yet, also the macroblock pathway is explained

below for the sake of completeness. All the images were transformed to the in-vivo space with the axial in-vivo T2w-image as a reference. To be able to perform correct resampling, the intensity values of all the input images were rescaled to [0 255]. Below, every step of the registration procedure is explained.

3D macroblock

In a first step, a 3D stack of the separate macroblock images was constructed. The user had to indicate the anterior of the glass plate containing the macroblocks, and some landmarks. A first registration of the slices was calculated with the Elastix software based on these landmarks [28]. The optimization criterion was normalized mutual information. Next, some seed points needed to be selected to segment the background using region growing. Then, after indicating slices from apex to base, a second registration resulted based on the contours of the macroblocks. Both registrations were compared and the best one was selected. The above steps had to be performed for every plate. Lastly, to come to the final stack, the background of the whole stack was removed and for every slice the apical or basal view was kept, depending on which one showed the least overhanging edges [59]. To better understand the concept of macroblocks, figure 4.3 provides an illustration of this registration step. For the next registration steps, illustrations are given in appendix A.

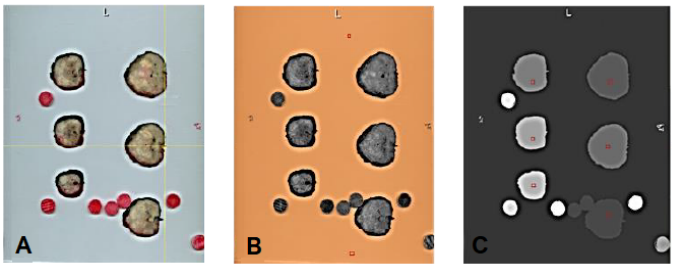

FIGURE 4.3: Illustration of the different steps in '3D macroblock'. The first step indicated the anterior of the glass plate containing the macroblocks and some landmarks. In the second step, the background was segmented using region growing. Thirdly, slices needed to be selected from apex to base. Adapted from [34].

Ex-vivo to in-vivo

The next step registered the ex-vivo T2w-image to the in-vivo T2w-image. This was done by matching the molds and thus performing a simple rigid registration. Normalized mutual information was used as a metric. The user had to indicate the back landmarks of the mold and its lower side as initialization. Then, corresponding slices were sought based on the shape of the mold. In the ex-vivo T2w-images, the shape of the mold was possibly distorted in the most upper and lower slices.

Therefore, the deformed slices could be excluded such that they did not influence the registration result. The ex-vivo 3D-image and ADC- or T2-map were then afterwards also warped to the in-vivo space by applying the found transformation [59].
To be able to match the molds in-vivo and ex-vivo, the mold had to be overlaid on the in-vivo image. Subsequently, a region of interest (ROI) that covered the mold was selected. This ROI had a size of approximately 235 x 235 pixels.

Macroblock to in-vivo

The 3D macroblock stack, created in step one, was registered to the in-vivo T2-image in this step. The mold or either the segmentations could be used to define the ROI of the in-vivo scan. When possible, always the mold was used. The user then had to visually select corresponding slices based on pathologic indications on the cutting-template paper. The registration was then executed using normalized mutual information as a metric. The transformation was subsequently checked and landmarks could be indicated manually to improve the result [59].

Tumor segmentation

Next, tumor segmentations had to be extracted from the histology sections. Predefined pathological regions, encircled by a dotted line, were manually delineated on every slice. In the following step, these segmentations were transformed to the in-vivo space together with the histology images [59].

Histology to ex-vivo and macroblock

Having completed the previous subtasks, the ex-vivo images and macroblocks were now already warped into the in-vivo space. Thus, registering the histology scans to the ex-vivo scans and macroblocks, also transformed these to the common in-vivo space. A b-spline non-rigid transformation was used here because the histology slices possibly were deformed during the slicing process. Again, normalized mutual information was used as optimization criterion. First, the most apical macroblock slice had to be selected. Then, the user had to select the inside of the mold by clicking within the prostate tissue on every slice in the image stack. When the prostate size was a little bit overestimated from the in-vivo scans, the mold could be a little too large. This leaded to gaps, filled with fixation fluid in the ex-vivo scans. Therefore, these gaps had to be colored, using region growing, to prevent the histology edge to be drawn to the mold edge instead of the prostate edge [59]. To match the stack size of the ex-vivo with that of the in-vivo images, empty slices were added in front and at the back of the ex-vivo stack. Next, the right and anterior of each histology slice had to be indicated and a coarse ROI was drawn around the histological tissue. The registration was calculated and evaluated. Again landmarks could be indicated

manually to improve the result [59].

Functional images

As can be seen from the list of registration inputs, one ex-vivo functional image (ADC- or T2-map) could be specified at the beginning of the registration process. However, most often there was more than one parametric ex-vivo image available. This final step in the registration process allowed to transform these extra parametric maps. Since the prostate specimen did not move during ex-vivo scanning, the ADC- and T2-maps were supposed to be intrinsically registered to the ex-vivo T2w-image. Therefore, the registration to the in-vivo space could be done by simply applying the transformation found in the 'Ex-vivo to in-vivo' step [59].
Figure 4.4 shows an example of the result of all registration steps.

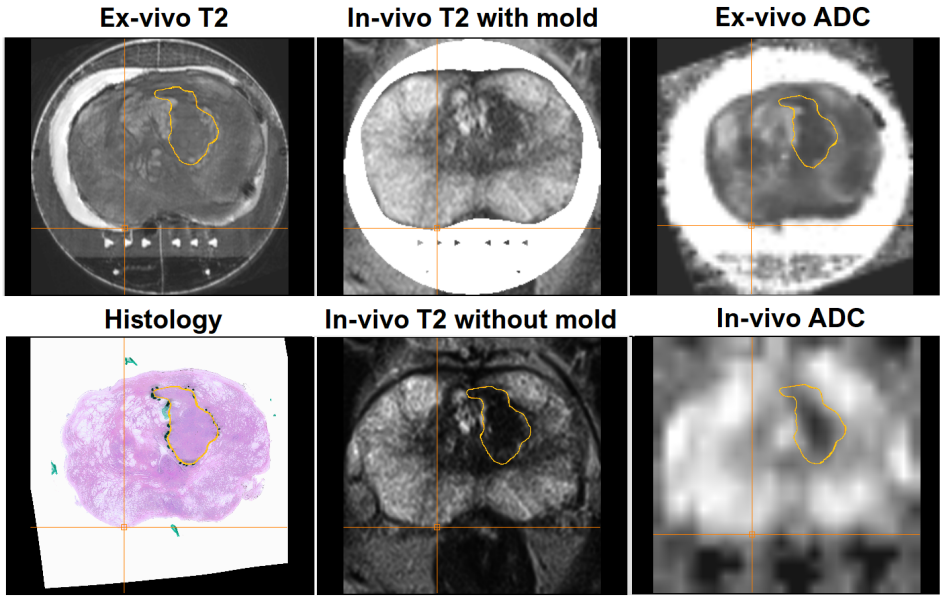

FIGURE 4.4: Example of result of registration. The macroblock registration is not included. It can be clearly noted that the segmented tumor region appears hypointense on the in-vivo T2-image and on both the in-vivo and ex-vivo ADC-map.

Intensity scaling

As mentioned above, all the images in the tool were rescaled to the range [0 255] in order to allow a consistent resampling. However, to be able to perform a representative quantification of the parametric maps, the original values were needed. They could be retrieved using the following formula:

$$V_{or} = V_{scal}/255 * S_{reg} \tag{4.3}$$

Where V_{or} is the original value, V_{scal} is the rescaled value and S_{reg} is the scaling applied by the registration tool. For the in-vivo ADC-image, S_{reg} simply equaled the maximum value of the original image. However, this was not true for the ex-vivo parametric maps, since a first resampling step already preceded the rescaling. The correct scale factor could then be found in the internal network of the DrTherapat tool. For every ex-vivo functional image, S_{reg} had thus to be manually looked up and written down. Note that thus a double scaling correction was needed: one to correct for the scaling after export (see subsection 4.2.2) and one to account for the rescaling during registration. Table 4.3 summarizes the details.

4.3.3 Identification of registration results

After the registration, the transformed images were saved as DICOM/TIFF in a results folder. Aside from transformation parameters and intermediately saved results, this folder contained the registered in-vivo T2w-image with and without mold, ex-vivo T2w- and 3D-image, all the parametric maps, histology image and tumor segmentations, available as cso and binary DICOM image. As explained in the previous subsection, the mold was overlaid on the in-vivo images during the registration procedure and a ROI around it was selected. Therefore, the outputted in-vivo T2w-image had a matrix size of approximately 235 x 235 and the in-vivo ADC-image of about 24 x 24 pixels. These sizes could vary slightly depending on the exact ROI selected. Since the ex-vivo T2w-image was resampled to the in-vivo T2-grid, it correspondingly had the same size. All the ex-vivo parametric maps however kept their original size, since their registration only included an affine transformation without using the Elastix software to resample to the reference grid. The histology and segmentation images had a size of (approximately) 1518 x 1518 pixels.
Further as explained above, the resulting images were scaled and the ex-vivo scans contained empty slices in front and at the back. These two facts were important to keep in mind during quantification.

4.4 Ex-vivo workflow: quantification

Quantification was done such that the objectives posed in the introduction could be investigated. This means that in-vivo and ex-vivo ADC-values and ex-vivo T2-values were quantified in tumor and control regions. This was done for all the in-vivo and ex-vivo parametric maps, including images acquired on both the 7T and 9.4T scanner and images acquired at multiple fixation times. The mean, standard deviation, minimum, maximum, number of voxels, area and volume were calculated for each region.

4.4.1 Generation of segmentations for control tissue

The registration process produced tumor segmentations, but no delineations for control regions. In order to be able to compare quantified values for tumor and healthy tissue, extra control regions had to be defined. Hereto, a module in MeVislab was created that allowed the user to manually draw cso's, using a spline function (see appendix A for illustration). They were constructed on the histology scans, such that certainly no overlap existed with the tumor regions. For each slice that contained at least one cancerous region, two control delineations were created: one in the PZ and one in the TZ. The shape of the regions was chosen by the user based on the histology image.

4.4.2 Labeling of segmentations

After constructing the control regions, tumor and control segmentations were now available as cso's. The next step was to assign labels to every cso on each slice. In that way, a quantification per region and not only per slice could be realized. Afterwards, the labeled cso's had to be converted to images, in order to be able to overlay the segmentations with the object images. A dedicated MeVislab module was written which numbered the delineations per slice, starting from one to the total number of regions present on the slice (see appendix A for illustration). The resulting labeled segmentation images were saved and could be consulted later on to recheck the numbering.

4.4.3 Extraction of scaling vectors

During the project workflow, the images underwent two scalings: one during export from the scanning device and one during registration. For the scaling during registration, it was already explained above how to correct for it for the in-vivo as well as for the ex-vivo images. The scale factor was constant for each image type. On the other hand, the factor applied during export was constant for the raw images but slice-specific for the calculated parametric maps. However, this was only true for the ex-vivo scans, since the in-vivo scans had a standardized scale factor of 10^{-6}. For the ex-vivo images, a Matlab script was used to extract the (slice-specific) scale factors from the source DICOM files. It outputted scaling vectors, containing the corresponding scale factors. These vectors could be used later on during quantification to correct for the scaling after export. Table 4.3 summarizes the characteristics of both scalings.

4.4.4 Quantification of object images

Quantification was done on 2D slices for the in-vivo as well as for the ex-vivo parametric maps using Matlab. From subsection 4.3.3 it became clear that not all the images had the same matrix size after registration. Therefore, a resampling step was needed. Every image was resampled to the in-vivo T2 matrix size, using bilinear interpolation. For the segmentation images, nearest neighbour (NN) interpolation

Table 4.3: Overview of the double scaling encountered in processing the prostate images: a scaling during export and a scaling during registration. The main characteristics of both are listed.

Scaling during export	**Scaling during registration**
- Constant scale factor for raw images - Slice-specific scale factor for parametric maps	Constant scale factor for every image type
Found in source DICOM headers for ex-vivo images	Found in network of registration tool for ex-vivo images
$= 10^{-6}$ for in-vivo images	= maximum of original in-vivo image for in-vivo images

was applied in order to preserve the binary fore - and background values. Once resampled, the tumor and control segmentations were overlaid on the parametric maps and per region the following parameters were calculated: mean, standard deviation, minimum, maximum, number of voxels, area and volume. Using the manually noted registration scale factors and the extracted scaling vectors, the values were brought to their standardized units: ms for the T2-maps and $10^{-3}mm^2/s$ for the ADC-maps. The area was expressed in mm^2 and the volume in mm^3. The results were outputted as Excel-sheets, containing also the segmentation labels. In that way, it was easy to check which result belonged to which region. Furthermore, the script saved the corrected (resampled and scale-corrected) parametric maps and segmentation images as Matlab files. These could be useful for future thesis students.

4.4.5 Statistical analysis

For certain slices, the quantified tumor zone was very small. Since the quantification of small regions was less reliable due to the partial volume effect and an increased sensitivity to registration errors, only lesions with an area greater than a threshold value were included in the statistical analysis. This threshold was defined according to the research of Borren et al. [60], who only analyzed lesions greater than three pixels on the in-vivo ADC-image. Applying this to the current study, only tumor regions with an area greater than $A_{min} = 22.43\ mm^2$ were retained. Depending on whether the tumor region was located in the PZ or TZ, the corresponding PZ or TZ control region was selected for each slice. Furthermore, it was possible that the delineations of tumor and/or control regions near the prostate boundary lay partly outside the prostate due to small registration errors. This was checked for every region on every object image based on a visual inspection of the segmented images. Figure 4.5 illustrates this with an example (more illustrations are given in appendix C). Regions lying for too large a part outside the prostate or in fixation fluid, such that they

did not represent true prostate tissue, were additionally excluded. Also, the visual inspections of the segmented images were used as a sanity check to verify whether the obtained values from quantification were feasible. It can be for example noticed from figure 4.5 that the tumor appeared hypointense on the ex-vivo ADC-image.

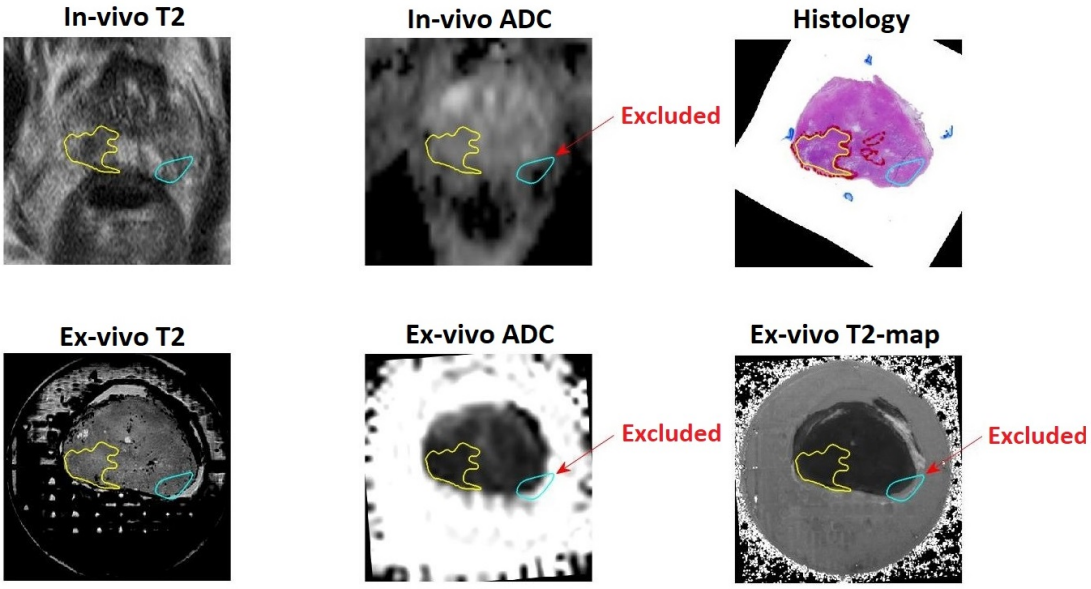

FIGURE 4.5: Example of registered object images overlaid with the corresponding segmentations. Tumor segmentations are yellow, control segmentations cyan. Since in this case the control region lies for a large part outside the prostate for the in-vivo ADC, ex-vivo ADC and T2-map image, it was excluded for these object images.

For every region included in the statistical analysis, the mean T2- and ADC-values per region were used to: investigate the influence of fixation time and magnetic field strength of the scanner, examine whether there was a difference in ADC-values obtained from the different ex-vivo diffusion-weighted protocols, compare healthy tissue with tumor tissue, find out how quantification in the TZ differed from that in the PZ and to compare in-vivo with ex-vivo ADC-values.

Figure 4.6 displays the histograms of T2- and ADC-values over all tumor and control regions of one patient. It can be clearly noted that both the T2- and ADC-values showed a positively skewed distribution. The same distribution was found in individual regions. Therefore, to test statistical significance, a Mann-Whitney U-test was used. This non-parametric test did not require the assumption of a normal distribution and checked whether there was a statistical difference between the medians (and not means) of two populations [61]. A p-value < 0.05 was considered to be statistically significant.

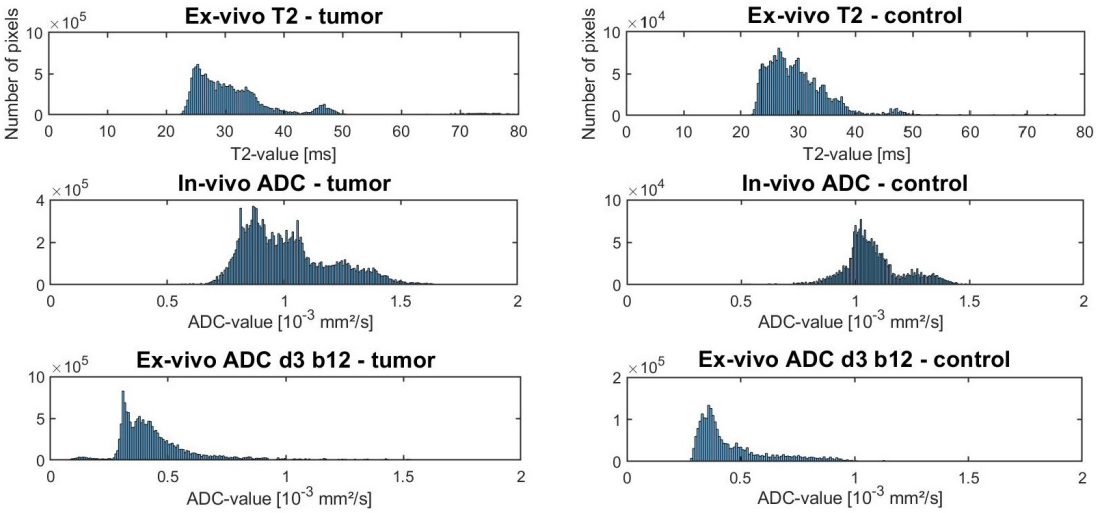

Figure 4.6: Example of histograms of T2- and ADC-values for one patient, calculated over all the tumor and control regions.

Chapter 5

Results

5.1 Patient population

A total of fifteen patients with biopsy proven prostate carcinoma was included in the study. They underwent in-vivo and, after radical prostatectomy, also ex-vivo mp-MRI. DWI was performed both in-vivo and ex-vivo whereas T2-mapping was only performed ex-vivo. The subjects had an average age of 58, PSA level of 8.76 ng/ml, Gleason score of 7 and tumor volume of 4.36 ml. The tumors were mostly located in the PZ. Table 5.1 provides a detailed overview of the clinical characteristics for every subject.

Table 5.1: Overview of clinical characteristics for every patient included in the study.

Pat	**Age** [*years*]	**PSA level** [*ng/ml*]	**cT-staging**	**pT-staging**	**N-staging**	**Gleason score**	**Tumor zone**	**Tumor volume** [*ml*]
1	60	4.45	cT2	pT2	Nx	3+4 = 7	PZ	2.2
2	60	6.75	cT1	pT2	Nx	3+4 = 7	PZ	3.3
3	51	7.58	cT2	pT3	Nx	3+4 = 7	PZ	3.4
4	71	5.32	cT2	pT2	Nx	3+4 = 7	PZ	3.3
5	47	5.68	cT2	pT2	N0	4+3 = 7	PZ	1.4
6	47	17.77	cT1	pT2	Nx	3+4 = 7	PZ	7.8
7	56	4.06	cT2	pT2	Nx	3+4 = 7	PZ	2.7
8	68	19.69	cT2	pT2	Nx	3+4 = 7	PZ	0.9
9	67	6.60	cT1	pT2	Nx	3+4 = 7	TZ	3.9
10	63	5.14	cT2	pT2	Nx	3+4 = 7	PZ + TZ	4.4
11	59	14.10	cT2	pT3	Nx	3+4 = 7	PZ + TZ	3.8
12	58	8.70	cT2	-	N0	4+3 = 7	TZ	4.1
13	55	8.05	cT3	pT2	Nx	3+4 = 7	TZ	11.8
14	56	6.50	cT2	pT3	Nx	3+4 = 7	PZ	9.3
15	52	11.00	cT2	pT2	Nx	3+4 = 7	PZ	3.1

5.2 In-vivo and ex-vivo imaging

In-vivo imaging resulted in a T2w-scan in three orthogonal planes and an axial diffusion scan for each patient. Image characteristics were according to table 4.1, except for subject 15 (see subsection 4.1.2).
Table 5.2 shows which ex-vivo scans were done for which patient. It also shows the scanner type used for imaging and the total fixation time before the first scan. Further, it indicates for which subjects multiple acquisitions at different fixation times were done. For these subjects, the time between the subsequent functional scans can be found in table 5.3. The ex-vivo image characteristics were as mentioned in table 4.2.

Table 5.2: Overview of which ex-vivo scans were done for each patient. If known from the scan reports, the third column indicates the fixation time before the first scan. In the DWI/DTI column, the 'd' stands for the number of directions and the 'b' for the number of b-values. When multiple acquisitions were done, this is indicated with the number of acquisitions in front of the 'X'.

Pat	**7T/9.4T**	**Fixation time** [*hours*]	**2D**	**3D**	**DWI / DTI**								**T2-map**
					d1 b15	**d3 b6**	**d3 b8**	**d3 b12**	**d5 b6**	**d6 b1**	**d6 b3**	**d6 b4**	
1	9.4T	42	X	X				X		X	X		X
2	9.4T	42	X	X				X		X	X		X
3	9.4T	72	X	X				X		X			X
4	9.4T	96	X	X				X		X			X
5	9.4T	96	X	X				X		X	X		X
6	9.4T	96	X	X				X		X	X		X
7	9.4T	?	2X	X				X		X	X		X
8	7T	?	2X	X		X							X
9	9.4T	120	X	X				X		X	X		X
10	9.4T	168	X	X				X		X	X		X
11	7T	?	X	X			X						X
12	7T	?	2X	2X	2X				2X			X	2X
13	9.4T	48	2X	2X				2X		2X	2X		3X
14	7T	1.5	2X	X		3X							3X
	9.4T	27	2X	3X				6X		3X	3X		7X
15	7T	?	X	X		X							X
	9.4T	?	X	X				X		X	X		X

TABLE 5.3: Time between the multiple functional acquisitions for patients 12, 13 and 14. The added time is always relative to the first acquisition.

Pat	Image type	2	3
12	d1b15	+16h	
	d5b6	+16h	
	T2-map	+18h	
13	d3b12	+15h	
	d6b1	+15h	
	d6b3	+15h	
	T2-map	+15h	+30h

Pat	Image type	2	3	4	5	6	7
14 (7T)	d3b6	+10h	+170h				
	T2-map	+10h	+170h				
14 (9.4T)	d3b12	+14h	+34h	+72h	+82h	+92h	
	d6b1	+14h	+72h				
	d6b3	+14h	+72h				
	T2-map	+11h	+24h	+36h	+72h	+84h	+92h

5.3 Registration and quantification

Registration was successful for all subjects. However for patients 1, 2 and 3, extra preprocessing steps were needed. Since for these cases, the original 2D T2w-image was distorted, a new 2D-image had to be constructed from the 3D-image. This reconstructed 2D-image consequently had a matrix size of 360 x 360 pixels (see table 4.2) and a different number of slices compared to the original 2D-image. For the parametric maps to have the same number of slices, the best matching slices of the parametric maps were visually selected. In that way, a resampling in the third dimension was avoided, which would have led to serious distortion of the prostate shape in some slices. Since the number of slices of the parametric maps was now reduced, their scaling vectors had to be adapted correspondingly.

For the quantification, the calculated mean T2- and ADC-values were benchmarked against typical values found in literature (table 2.5). For patient 8, the in-vivo ADC-values were abnormal due to the presence of rectal gas during in-vivo DWI. Other deviating values could be ascribed to small registration errors (see figure 4.5). However, these cases were not included in the statistical analysis of the results.

5.4 Statistical analysis

Table 5.4 shows per patient how many 2D (slice by slice) tumor lesions were retained for the statistical analysis, after rejecting lesions with an area $< A_{min}$ (as defined in subsection 4.4.5) and lesions that lay for a large part outside the prostate due to registration errors. For patient 8, there were no lesions larger than A_{min}. Depending on whether the tumor region was situated in the PZ or TZ, the corresponding PZ or TZ control region was selected for each slice. If a slice contained both lesions in the PZ and in the TZ, both control regions were retained. The mean T2- and ADC-values of the selected tumor and control regions were used to investigate the research questions below. Figures and tables are given at the end of the section to keep a clear overview.

5.4.1 Influence of fixation time

This analysis was performed separately for both scanner types. First, the mean ex-vivo T2- and ADC-values at multiple fixation times were investigated for patients 13 and 14 on the 9.4T scanner. Additionally, the same was done on the 7T scanner for patient 14, to examine extreme fixation times (ranging from 1.5h to 170h). The analysis was done for both tumor and control regions, but since their trend was similar, only results for tumor regions are presented. For the 9.4T scanner, only the ADC-values of the *d3b12*-protocol (three directions, twelve b-values) are shown, since the trend for the other DWI protocols was similar.

Figure 5.1 shows boxplots of the mean ex-vivo T2- and ADC-values at multiple fixation times for patients 13 and 14, scanned on the 9.4T scanner. As can be noted, there was not much change in the ADC-values over several fixation times. The T2-values however fluctuated, but no clear trend could be identified. In patient 14, the T2-values showed at first a downward trend, but at longer fixation times the values slightly rose again.
When looking at more extreme fixation times in patient 14 on the 7T scanner (figure 5.2; note the different scale of the y-axis for the T2-values compared to figure 5.1), both T2- and ADC-values decreased rapidly after early fixation. Then, 170 hours later, the ADC-values had further decreased slightly, whereas the T2-values had further decreased strongly. To investigate these observations more in depth, the right side of figure 5.2 displays the histograms of the subsequent T2- and ADC-values for patient 14. The distribution of the ADC-values did not vary much over time, whereas that of the T2-values evolved from a spread distribution towards a more centered one.

5.4.2 Difference between ex-vivo DWI protocols

Ex-vivo DWI was performed following multiple protocols in this project, involving different numbers of directions and b-values. To investigate the influence of the protocol on the ADC-values, figure 5.3 shows for the tumor regions of one patient (13) a comparison between the three DWI protocols of the 9.4T scanner together with the corresponding DWI fitting curves for calculation of the ADC-values. The median of the ADC-values obtained with the *d6b3*-protocol was significantly higher ($p = 0.029$, Mann-Whitney U-test) than that of the ADC-values obtained with the *d6b1*-protocol, which in turn had a significantly higher median ($p = 0.029$, Mann-Whitney U-test) than the ones obtained with the *d3b12*-protocol.

To verify this observation, a further analysis was done for all the tumor regions of patients 1, 2, 3, 4, 5, 6, 7, 10, 14 and 15, scanned on the 9.4T scanner (figure 5.4). Contrary to the 7T, the 9.4T scanner had fixed DWI protocols and thus provided the most homogeneous data set. Note that only tumor regions in the PZ were selected, to exclude possible differences between ADC-values in the TZ and PZ. A possible influence of unequal fixation time until the first scan between the different patients

was neglected. Again, ADC-values obtained from the *d6b3*-protocol were significantly higher than those from the *d6b1*-protocol and *d3b12*-protocol. P-values can be found in figure 5.4.

5.4.3 Influence of magnetic field strength

Since both patient 14 and 15 were scanned on the 7T as well as on the 9.4T scanner, their tumor regions were used to investigate the influence of the magnetic field strength of the ex-vivo scanner. DWI on both scanners was not done according to the same protocol. ADC-values of the *d3b6*-protocol on the 7T were compared to the ADC-values of the *d6b1*-protocol on the 9.4T scanner to match the range of b-values as closely as possible: [0 2000] s/mm^2 versus [0 1500] s/mm^2, see table 4.2. T2-values could be compared unambiguously. For each patient, the T2- and ADC-maps at both scanners were selected that were scanned at the closest matching fixation time. Figure 5.5 depicts the results. For patient 14, the T2-values but not the ADC-values were significantly different for both scanners. At first sight, there seemed to be a difference in T2- as well as in ADC-values for patient 15. However, due to the small sample size (patient 15 included only three lesions, see table 5.4) these differences were not significant.

In order to have a larger sample size, the analysis was additionally performed across different patients. For the 9.4T scanner the PZ tumor regions of patients 1, 2, 3, 4, 5, 6, 7, 10, 14 and 15 were selected. For the 7T scanner the PZ tumor regions of patients 14 and 15 were selected, since the other patients scanned on the 7T had either TZ tumor lesions or different DWI protocols. The comparison is visualized in figure 5.6. In this case, again the T2-values but not the ADC-values were significantly lower on the 9.4T than on the 7T scanner.

5.4.4 Healthy versus tumor tissue

It became clear from the previous subsection that T2-values depend on the scanner field strength. Therefore, the comparison of T2- and ADC-values in healthy versus tumor tissue was done only for the 9.4T scanner since the majority of the patients was scanned on this device. The values in the PZ tumor regions were compared to those in the PZ control regions for patients 1, 2, 3, 4, 5, 6, 7, 10, 14 and 15 in figure 5.7. As can be noted, ADC-values were significantly higher in healthy tissue than in tumor tissue, both in-vivo and ex-vivo (for all the different protocols). Ex-vivo T2-values, although these tended to be higher in tumor than in healthy tissue, were not significantly different.

Peripheral versus transition zone

An analogous analysis was done on the 9.4T for patients 9, 10 and 13, having lesions in the TZ. For this case, the boxplots are not visualized but only the p-values are given (again obtained from the Mann-Whitney U-test). The ex-vivo T2-values in the

TZ were not significantly different in tumor compared to healthy tissue ($p = 0.505$). The in-vivo ADC-values in the TZ were however significantly higher in healthy versus tumor tissue ($p = 0.027$). The same was true for the ex-vivo ADC-values in the TZ (for all the protocols) with each a p-value of $p < 0.001$. The average T2- and ADC-values for tumor and healthy tissue are summarized in table 5.5 for the PZ as well as for the TZ.

In-vivo versus ex-vivo ADC

Taken the different ex-vivo ADC protocols together, it can be seen from table 5.5 that the ADC-values decreased on average 53% ex-vivo compared to in-vivo for the PZ and 51% for the TZ. Further, in-vivo ADC-values dropped by 14% in tumor versus healthy tissue in the PZ and 15% in the TZ. For ex-vivo ADC-values, these rates were 17% and 31%. Consequently, tumor regions appeared hypointense on the in-vivo and ex-vivo ADC-maps (see figure 4.4).

TABLE 5.4: Overview of the lesions per patient included in the statistical analysis.

Pat	**1**	**2**	**3**	**4**	**5**	**6**	**7**
Number of 2D lesions	2	8	3	3	2	4	4
Number of 2D lesions in PZ/TZ	PZ: 2	PZ: 8	PZ: 3	PZ: 3	PZ: 2	PZ: 4	PZ: 4
Mean area $[mm^2]$	81.61	56.58	99.43	60.70	64.64	167.62	53.46

Pat	**9**	**10**	**11**	**12**	**13**	**14**	**15**
Number of 2D lesions	6	9	5	6	4	8	3
Number of 2D lesions in PZ/TZ	TZ: 6	PZ: 6 TZ: 3	PZ: 4 TZ: 1	TZ: 6	TZ: 4	PZ: 8	PZ: 3
Mean area $[mm^2]$	130.23	47.65	120.39	151.83	265.82	214.46	48.21

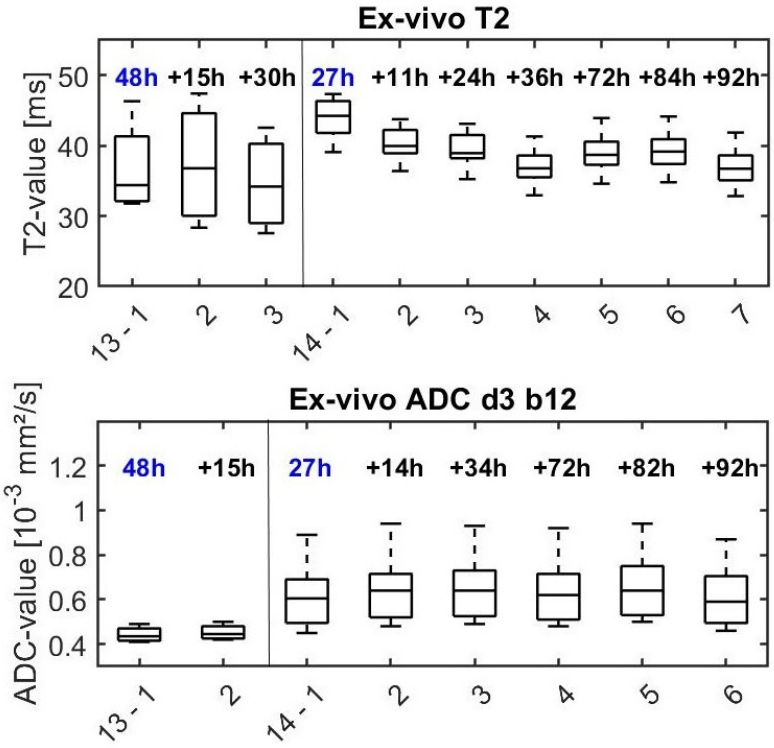

FIGURE 5.1: Boxplots of the mean ex-vivo T2- and ADC-values of the tumor regions of patients 13 and 14 at multiple fixation times, scanned on the 9.4T scanner. For each subsequent scan, the elapsed time relative to the total fixation time before the first scan (blue) is indicated above each boxplot.

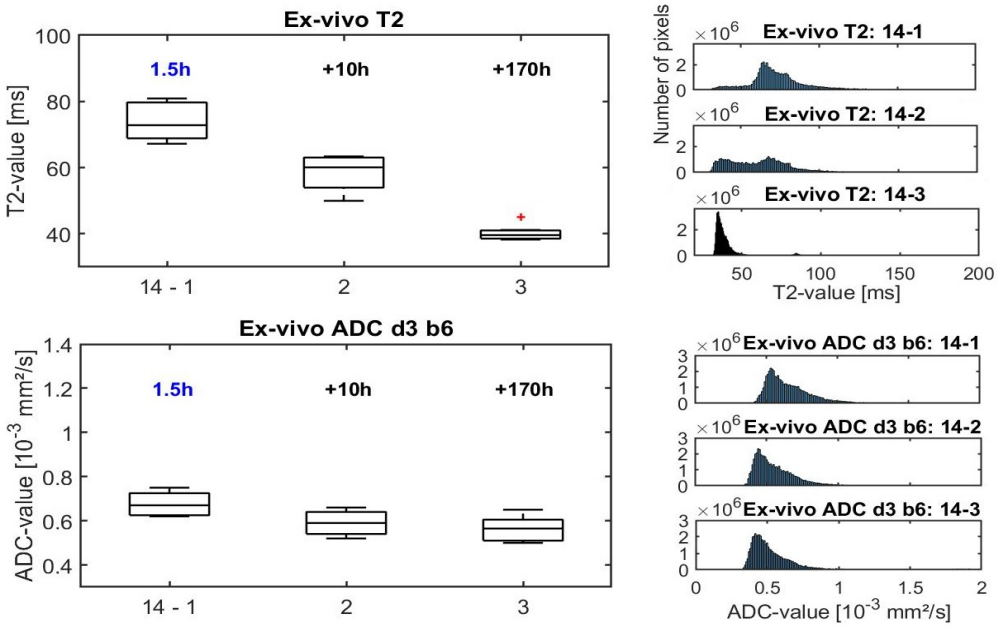

Figure 5.2: **Left**: boxplots of the mean ex-vivo T2- and ADC-values of the tumor regions of patient 14 at multiple fixation times, scanned on the 7T scanner. For each subsequent scan, the elapsed time relative to the total fixation time before the first scan (blue) is indicated above each boxplot. **Right**: histograms of the subsequent T2- and ADC-values, calculated over of all the tumor regions of patient 14.

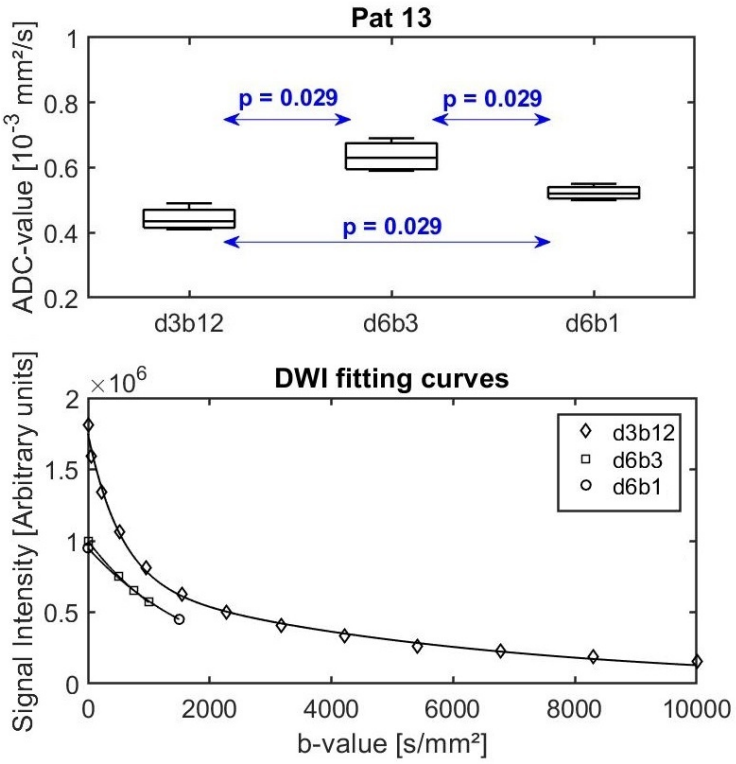

FIGURE 5.3: Comparison of the mean ex-vivo ADC-values of the tumor regions of patient 13, obtained with three different DWI protocols at the 9.4T scanner. The corresponding DWI fitting curves are shown in the lower panel.

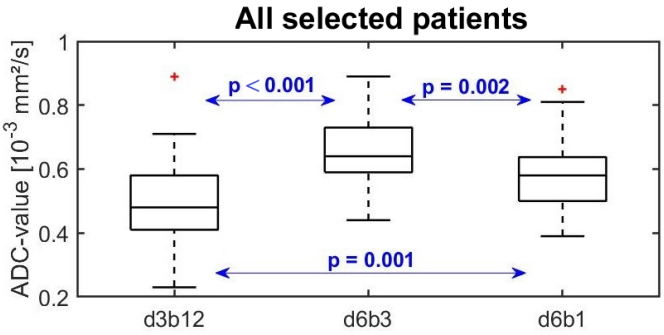

FIGURE 5.4: Comparison of the mean ex-vivo ADC-values of the tumor regions of patients 1, 2, 3, 4, 5, 6, 7, 10, 14 and 15, obtained with three different DWI protocols at the 9.4T scanner.

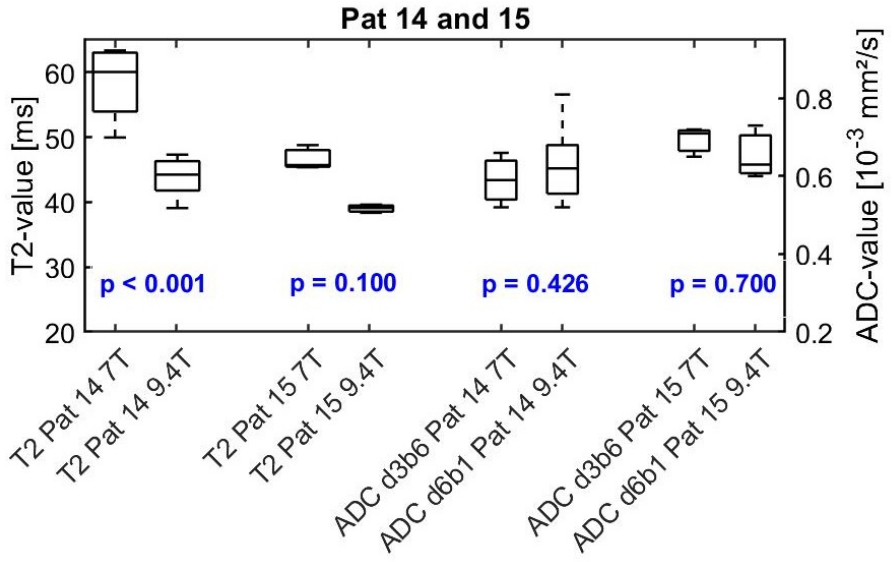

Figure 5.5: Boxplots of the mean ex-vivo T2- and ADC-values of the tumor regions of patients 14 and 15 at both scanner types.

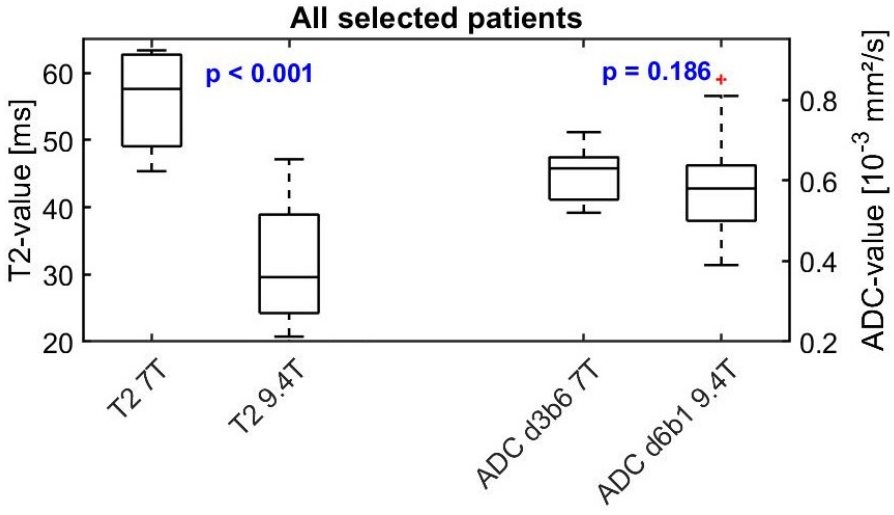

Figure 5.6: Boxplots of the mean ex-vivo T2- and ADC-values of the tumor regions of patients 1, 2, 3, 4, 5, 6, 7, 10, 14 and 15 for the 9.4T scanner and of patients 14 and 15 for the 7T scanner.

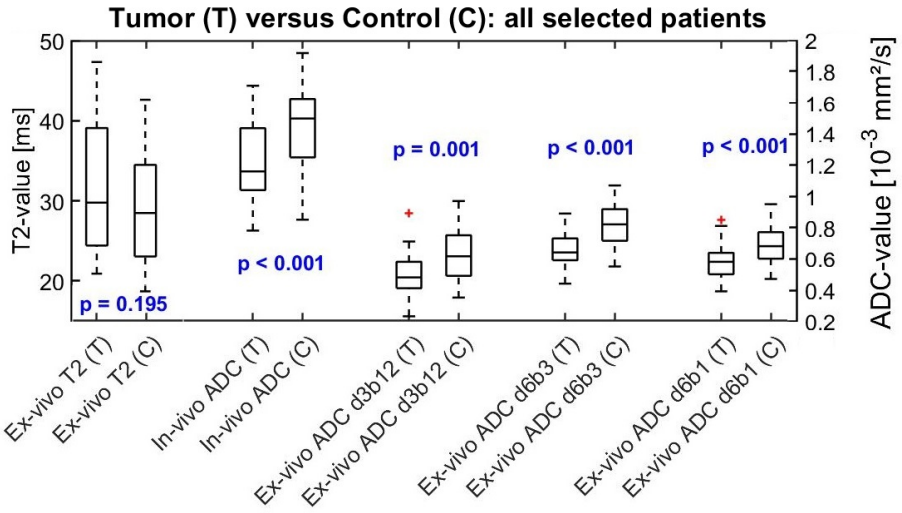

FIGURE 5.7: Boxplots of the mean T2- and ADC-values of the PZ tumor and control regions of patients 1, 2, 3, 4, 5, 6, 7, 10, 14 and 15.

TABLE 5.5: Summary of the average T2- and ADC-values found in tumor and healthy tissue, in the PZ and TZ.

Protocol	**Ex-vivo T2** $[ms]$	**In-vivo ADC** $[10^{-3}mm^2/s]$	**Ex-vivo ADC d3b12** $[10^{-3}mm^2/s]$	**Ex-vivo ADC d6b3** $[10^{-3}mm^2/s]$	**Ex-vivo ADC d6b1** $[10^{-3}mm^2/s]$
PZ tumor	31.62 ± 7.22	1.24 ± 0.18	0.50 ± 0.17	0.66 ± 0.18	0.58 ± 0.17
PZ healthy	29.06 ± 4.22	1.45 ± 0.15	0.62 ± 0.15	0.80 ± 0.15	0.68 ± 0.15
TZ tumor	31.11 ± 3.42	1.31 ± 0.26	0.50 ± 0.15	0.67 ± 0.17	0.54 ± 0.13
TZ healthy	32.10 ± 4.11	1.55 ± 0.20	0.76 ± 0.16	0.95 ± 0.19	0.77 ± 0.16

Chapter 6

Discussion

6.1 Recapitulation of the thesis scope

This study included fifteen patients to investigate the potential of mp-MRI as an emerging imaging technique for the detection and follow-up of prostate cancer. A patient-specific 3D prostate mold was used to facilitate histology to in-vivo MRI registration of histologically defined cancerous prostates with high-resolution ex-vivo MRI as an intermediate step. This provided a ground-truth that made it possible to quantify T2- and ADC-values from mp-MRI in order to distinguish tumor tissue from healthy tissue. More specifically, the focus of the presented thesis was on the analysis of the ex-vivo imaging data that were acquired during the course of this study. In the first place, issues regarding the processing of this data set had to be resolved, as this was at the start of this work still unexplored terrain. Changes in image characteristics when converted from one format to another had to be dealt with, the images needed proper preprocessing before being inputted in the registration tool, several issues with the registration tool itself had to be solved, the functional images had to be resized for quantification, the double scaling of the intensity values was addressed ... Once these issues were resolved, the influence of the magnetic field strength of the ex-vivo scanner and of the fixation time on the ex-vivo quantified parameters was investigated. Also, the different ex-vivo DWI protocols were compared and quantification in healthy versus tumor tissue was addressed. The following hypotheses were posed: 1) T2- and ADC-values will be lower for longer fixation times, 2) they will be similar on both scanner types, 3) they will decrease both in-vivo and ex-vivo in tumor tissue compared to healthy tissue and 4) they will decrease ex-vivo compared to in-vivo.

6.2 Interpretation of results

6.2.1 Influence of fixation time

Bourne et al. [39] show that T2- and ADC-values reduce significantly post- compared to pre-fixation. However, not much research is done yet on how the values evolve

with longer fixation times. Figure 5.2 confirms the conclusions of Bourne et al.: T2- as well as ADC-values decrease rapidly after fixation. From then, the decrease for both seems to go a lot slower with the ADC-values more or less stagnating, whereas T2-values show a fluctuating downward trend. The fixation process induces a change in tissue architecture and reduces the amount of free protons, thus causing lower ADC- and T2-values [46]. The stagnation of ADC-values can possibly be explained by assuming that once the change in tissue architecture induced, longer fixation times will not alter the architecture further. The observed variation in T2-relaxation time could be attributed to a number of other factors than fixation alone, with the most important being RF nonuniformity, temperature, motion of the specimen between subsequent scans and transmitter nonlinearity [62]. The effect of the formalin fixation will thus probably become less dominant compared to these other effects over time and the influence on the T2-values will become less outspoken. In conclusion, it can be stated that there is a drop in T2- as well as in ADC-values immediately after fixation, but that this downward trend attenuates for longer fixation times (especially for ADC-values). The hypothesis that T2- and ADC-values will be lower for longer fixation times is thus partly confirmed.

6.2.2 Difference between ex-vivo DWI protocols

From subsection 5.4.2 it became clear that the *d6b3*-protocol yields the highest ADC-values, followed by the *d6b1*-protocol and then the *d3b12*-protocol. This observation can be explained by looking at the b-values used for fitting (table 4.2). Including b = 0, the ranges of b-values are respectively [0 1000], [0 1500] and [0 10000] s/mm^2. Bourne et al. [40] show that for an extended range of b-values (up to 4897 s/mm^2), the diffusion decay follows a bi-exponential trend due to the 'the compartmentation of water in physically separate microenvironments with distinct diffusion properties'. This suggests that prostate tissue is built up out of distinct cell types (compartments) with each their own characteristic diffusion properties. Figure 5.3 confirms these findings: due to the wide range of b-values, the *d3b12*-protocol exhibits bi-exponential decay and therefore overall smaller ADC-values. Further, since the bi-exponential behavior seems to initiate from a b-value of approximately 1000 s/mm^2, it can be now understood that the *d6b3*-protocol will yield even higher b-values than the *d6b1*-protocol. Despite the mutual difference between the protocols, their clinical relevance is not different: for each protocol the ADC-values are significantly lower in tumor tissue compared to healthy tissue (see below and figure 5.7).

6.2.3 Influence of magnetic field strength

To the best knowledge, no previous research has been conducted on the influence of the magnetic field strength of the scanner on ex-vivo T2- and ADC-values. When comparing ADC-values on different scanners, it is important that they originate from DWI protocols with approximately the same range of b-values, since this has a major influence (see previous subsection). From figures 5.5 and 5.6, it can be concluded that, when the named condition is fulfilled, ADC-values do not differ significantly

with the scanner type. On the contrary, T2-values do differ significantly with the magnetic field strength of the scanner: they are lower for a higher field strength. According to AD Elster [63], this decrease can be devoted to microscopic diffusion and susceptibility effects, which become dominant at very high field strengths (> 7T). The hypothesis that T2-values do not depend on magnetic field strength was based on low field strengths. At the encountered very high fields however, there does seem to be a clear difference.

6.2.4 Healthy versus tumor tissue

The last hypotheses, namely that T2- and ADC-values will decrease both in-vivo and ex-vivo in tumor tissue compared to healthy tissue and that they will decrease ex-vivo compared to in-vivo is confirmed in figure 5.7 for the ADC- but not for the ex-vivo T2-values. The range of the average in-vivo and ex-vivo ADC-values found in table 5.5 corresponds well with typical values found in literature (table 2.5). The ex-vivo T2-values however are almost a factor 2 smaller than those found in a previous thesis report by M. Glorieux [34]. One possible explanation is that in the mentioned thesis, only low grade prostate cancers were considered, having possibly higher ex-vivo T2-values. Also in that thesis, no significant difference between healthy and tumor tissue was found in terms of ex-vivo T2-values. In conclusion, it can be stated that ADC-mapping has much more discriminative power than T2-mapping to distinguish healthy from cancerous prostate tissue. Whereas the above observations yield for the PZ, the same is observed for the TZ (table 5.5). T2- and ADC-values are slightly higher in the TZ than in the PZ.

6.3 Strengths and limitations

6.3.1 Strengths

The major obstacle that impedes correlation of in-vivo mp-MRI with an histological ground-truth is the registration of both. It is hindered by the low out-of-plane resolution of the in-vivo images and the lack of 3D information. Although there is abundant literature available, few use an accurate 3D registration solution. Many registration methods are rather heuristic in finding matching slices and eventually need a 3D transformation to register the histology sections to the in-vivo MRI-images [26][27]. Since registration is always prone to small interpolation and alignment errors, high-dimensional transformations should be avoided. An improvement has been the use of prostate molds to facilitate registration. This project involves a further major improvement by using a patient-specific 3D prostate mold with high-resolution ex-vivo MRI-images as an intermediate step. Additionally, the mold contains specific features to assure precise position of the excised prostate in the mold. This reduces the registration problem from 3D to 2D, which should be much more accurate and provide a good basis for quantification.

Next, the double scaling issue was resolved and T2- and ADC-values were quantified in their standardized units. Although this may seem evident, the scaling issue was hard to address. The ex-vivo imaging data was an untouched data set and also the outputs of the registration tool were never examined in depth before. Solving by extension all the problems encountered in the ex-vivo workflow (see section 6.1) was a matter of first discovering the problems and then to solve them in an adequate way.

Further, this study is among the first to investigate the influence of the magnetic field strength of the scanner and the influence of extent of fixation time on ex-vivo T2- and ADC-values. Although the results of the influence of fixation time were a bit unpredictable, they could be substantiated by reasonable arguments. The results of the influence of scanner type were completely consistent with literature. Additionally, it became clear that there is a difference in ADC-values coming from different ex-vivo DWI protocols. This may provide more insight to come to a standardized DWI protocol when imaging future specimens.

6.3.2 Limitations

One limitation of using a registration mold is that the excised prostate should fit. When in-vivo the prostate was deformed due to the presence of rectal gas, filling of the bladder or due to breathing, the reconstructed mold based on the in-vivo T2w-images would not represent the true prostate shape. In this case, the specimen would not fit in the mold. In this study, this occurred 5 times for in total 26 patients, i.e. in about 19 % of the cases. These cases could then not be used for further analysis, as the registration between histology and in-vivo and ex-vivo images could not be performed. Another limitation was the DrTherapat registration tool that was used for the in-plane 2D registration. Although all the registrations in this project were successful, the tool often needed manual interventions in order to produce a satisfying result. A more automated procedure would save a lot of time. Also, the result sometimes yielded segmentations that lay for a large part outside the prostate. They had to be excluded from the study. To minimize the effect of these registration errors and of partial volume effects, only lesions that were sufficiently large (area $> A_{min}$, see subsection 4.4.5) were included in the statistical analysis.

Next, there was large heterogeneity in the (imaging) data. First, tumors were mostly localized in the PZ, but in some cases also in the TZ. Then, the fixation times until the first scan and between subsequent scans were different for every patient. Further, only two patients were scanned on both scanners. Also, the DWI protocols and their resolutions were different on both scanners. Lastly, for patient 1, 2, 3 and 15 the in-vivo images had deviating matrix sizes since the original scan was distorted or imaging happened externally. This all leaded to the fact that in some cases only few patients could be selected to address a certain research question. This was for example the case for the comparison of the scanner types, where primary the analysis

was only done for patients 14 and 15, scanned on both devices.

Also attention should be paid to interpolation artifacts. Since after registration, the parametric maps and segmentation images had a different matrix size than that of the in-vivo T2w-image, they had to be resampled. The downsampling of the segmentation images used NN interpolation in order to preserve the binary fore- and background values. This caused the edges of the segmentations to be a bit jagged. The parametric maps were resampled using bilinear interpolation. Since resampling always leads to an approximation of the true underlying intensity values, it should be avoided when possible. Therefore, it would be better that DWI at the 9.4T scanner could be performed at a higher resolution. Secondly, the registration tool needs adaptation such that all the registered images are outputted with an equal matrix size and such that an additional resampling afterwards is not required anymore.

A final limitation of this study is the fact that all the patients had the same Gleason score of seven. This made it impossible to correlate T2- and ADC-values with tumor grade. On the other hand however, this consistency in Gleason score did provide a certain degree of homogeneity in the performed analysis.

6.4 Implications and relevance

In the first place, this thesis confirms the potential of mp-MRI to provide a parameter set of biomarkers for the detection and follow-up of prostate cancer. More specifically, T2- and ADC-values are expected to reflect the underlying tissue density, being higher in tumor tissue. Consistent with literature, the ADC is found to be a more discriminative marker than the T2-relaxation time. However, the regional analysis of T2- and ADC-values is still a small part of the whole potential of mp-MRI (see next subsection). This study for example does not investigate small lesions. Yet, they are expected to show similar quantitative characteristics on mp-MRI compared to large lesions. Additionally, it are mostly the large lesions that are primary target of prostate cancer treatment methods since, given their potential for recurrence, they pose the biggest threat for the patient.
The potential of mp-MRI has to be put in contrast with its limitations. First, it does not have the power to replace biopsies: still, to come to a final diagnosis, prostate tissue has to be extracted and examined under a microscope. Mp-MRI however does have the power to guide these biopsies. Based on hypointense T2- and ADC-values, hotspots can be indicated that should be the primary target for biopsy. Next, in order for the images to be of sufficient quality, the field strength of the in-vivo scanner should be at least 1.5T [64]. Moreover, the image quality is susceptible to motion artifacts, including movements of the intestines. Additionally, it is influenced by the signal strength of the prostate, which can be low in obese patients since the receiver coil is in this case further away from the prostate [64]. Imaging should thus be performed adequately for mp-MRI to be of significant diagnostic use. Then, the interpretation of the functional information included in the images might be

subjective. It is important that the assessment happens by experienced clinicians and that, when possible, a second opinion is included.
Despite these limitations, the possibilities of mp-MRI can not be overlooked. As mentioned higher, it can be for example a great aid in the development of focal treatment therapies. The listed limitations are even expected to be overcome in the near future [64].

Besides confirming conclusions drawn in other research, this study also brings to light new results regarding the influence of the magnetic field strength of the scanner, extent of fixation time and DWI protocol. Although these results are valid, they should be handled with care since they were sometimes based on small sample sizes (see above). However, the delivered work does provide a good basis for future students to continue this research. Having knowledge of the described influences, it should be possible to acquire more homogeneous ex-vivo imaging data such that larger sample sizes could be attained in the future to verify and go beyond the posed conclusions.

Finally, the relevance of using ex-vivo MRI in addition to in-vivo MRI should be emphasized. Whereas in the future the goal is to assess prostate cancer aggressiveness based only on in-vivo mp-MRI, this technique first needs extensive validation. The primordial importance of ex-vivo MRI is thus to provide a high-resolution intermediate to improve the histology to in-vivo registration accuracy. From a second view, quantifying ex-vivo mp-MRI is very useful to check whether the same conclusions as in-vivo can be observed. From table 5.5 it is clear that ADC-values decrease in tumor tissue in-vivo and ex-vivo with a similar rate. With this, the observations in-vivo are strongly substantiated. This study did not include in-vivo T2-mapping, but when the in-vivo T2-values from table 2.5 are compared to the ex-vivo T2-values of this study, it can be seen that the difference between healthy and tumor appears to be much smaller ex-vivo than in-vivo. This observation needs further investigation.

6.5 Future perspective

Whereas this and most studies in literature first identify tumor regions on an histological ground-truth and subsequently quantify mp-MRI parameters for these regions, it would be very useful to do the reverse. It would be valuable to conduct a study wherein first possible tumor regions are identified on in-vivo ADC- and/or T2-maps and then to verify this on the histological ground-truth. This is also the way how mp-MRI is applied in clinical practice: based only on the in-vivo images, the clinician should get an idea of which prostate regions are indicative of malignancy.
Further, the current ex-vivo workflow, developed in this thesis, requires a reasonable amount of manual processing. Examples are preprocessing of the images prior to registration, generating control segmentations, labeling the segmentations, extracting scaling vectors and manually noting down the scaling factors applied during registration of additional functional images. A more automated procedure would speed up the whole process significantly. Given the complexity and variability in the workflow

however, the development of a completely automated procedure will be a serious challenge.
Another suggestion would be to include a sanity check for the result of registration. Since the in-house developed registration tool is not perfect, its shortcomings could be checked by evaluating the results in terms of a dice similarity coefficient. This would allow to more precisely assess the contribution of registration errors to the results of quantification.
Although quantification in this study was done on a regional basis, also a voxel-wise approach could be handled. This would allow to compare T2- and ADC-values one-to-one with the histological tissue density and to dig into the heterogeneity of the tumor lesion. Further, quantification was done in 2D, thus slice by slice. Another option could be to identify lesions on subsequent slices belonging to the same tumor. These lesions can then be combined into a volumetric analysis, comparing tumors rather than cross sections of tumors. Also, other histological stainings than the haematoxylin and eosin staining could be used. Immunohistochemistry staining for example can identify tumor tissue by antibodies binding to specific antigens present in different biological tissues [65]. Different stainings may thus yield additional information to identify malignant tissue.
Finally, major potential lies in the use of machine learning techniques and radiomics. This study focuses only on T2- and ADC-values. Additional parameters like the FA and diffusion kurtosis could be included to characterize anisotropic diffusion behavior. Other mp-MRI modalities like DCE-MRI and MRS could provide more biomarkers, like K_{trans}, Rwo, IAUC and citrate, creatine and choline concentrations. Radiomics are computer-extracted texture features that can be superior to intensity values of mp-MRI alone to characterize tumor tissue [66]. Besides signal intensities and first order statistics, radiomics include co-occurence features like autocorrelation, cluster prominence, contrast ..., Gabor features, and texture energy features [66][67]. In an advanced study, an optimal set of features could be identified and then used in a machine learning algorithm to automatically classify prostate tissue according to its degree of malignancy.

Chapter 7

Conclusion

Since prostate cancer is the fifth leading cause of cancer deaths in men, it is essential to keep track on developing new techniques towards detection, evaluation and monitoring of the disease [4]. This thesis investigated the potential of mp-MRI, more in particular T2- and ADC-mapping, as an emerging imaging technique for non-invasive tumor grading in prostate cancer. Whereas the potential is large, mp-MRI still needs profound validation. Therefore, in-vivo mp-MRI images were registered to an histological ground-truth, facilitated by ex-vivo mp-MRI as a high-resolution intermediate step using a patient-specific 3D prostate mold, in order to quantify T2- and ADC-values in cancerous and healthy tissue.
More specifically, the focus of the presented thesis was on the ex-vivo imaging data. In the first place, issues regarding the processing of this untouched data set were resolved. Major achievements were: the needed preprocessing of the images before being inputted in the registration tool was identified, issues with the registration tool itself were resolved, the needed resampling for quantification was identified and applied and the double scaling issue was addressed such that quantified values were presented in their standardized units. Hereafter, a 2D slice by slice quantification of T2- and ADC-values for tumor and control regions was done for fifteen patients in total. Control regions were extracted manually based on the histological images such that for each slice containing at least one tumor region, two control regions were generated: one in the PZ and one in the TZ. In this way, depending on whether the tumor region was located in the PZ or TZ, the corresponding control region could always be selected. After excluding lesions that were smaller than a specified threshold and regions that lay for a large part outside the prostate due to registration errors, the following research questions were statistically addressed: 'What is the influence of extended fixation times and of the magnetic field strength of the scanner on ex-vivo T2- and ADC-values?', 'How do ex-vivo ADC-values differ with the number of directions and b-values used in the acquisition protocol?' and 'How do T2- and ADC-values compare in healthy versus tumor tissue, in-vivo versus ex-vivo and in the PZ compared to the TZ?'. From the results it became clear that T2- as well as ADC-values decrease strongly immediately after fixation, but that this downward trend diminishes for longer fixation times (especially for ADC-values). Then, it was

found that the higher the b-values used for DWI, the lower the ADC-value. This could be explained by the bi-exponential diffusion decay due to water compartmentation in physically separate microenvironments for high b-values. Next, when the range of b-values was similar, the magnetic field strength of the scanner did not have a significant influence on the ADC-values. For fields above 7T however, T2-values significantly dropped with magnetic field strength due to microscopic diffusion and susceptibility effects. In-vivo and ex-vivo ADC-values were significantly lower in tumor tissue compared to healthy tissue, in the PZ as well as in the TZ. Ex-vivo T2-values however were not significantly different in the PZ nor in the TZ. T2- and ADC-values were slightly higher in the TZ compared to the PZ.
From the viewpoint of clinical practice, this thesis has reasonable relevance in the sense that it confirms the potential of mp-MRI to provide a parameter set of biomarkers that is able to distinguish tumor tissue from healthy tissue. Also for the future course of this project it has implications. This thesis provides the corrected (resampled and scale-corrected) parametric maps and segmentation images used for quantification, making a future more extensive analysis possible without having to run through all the image processing steps (scaling, registration ...) again. Having knowledge of the described conclusions, it should be possible in the future to acquire more homogeneous ex-vivo imaging data such that larger sample sizes could be attained to verify and go beyond the posed conclusions.

Appendices

Appendix A

Illustrations of registration steps and MeVislab tools

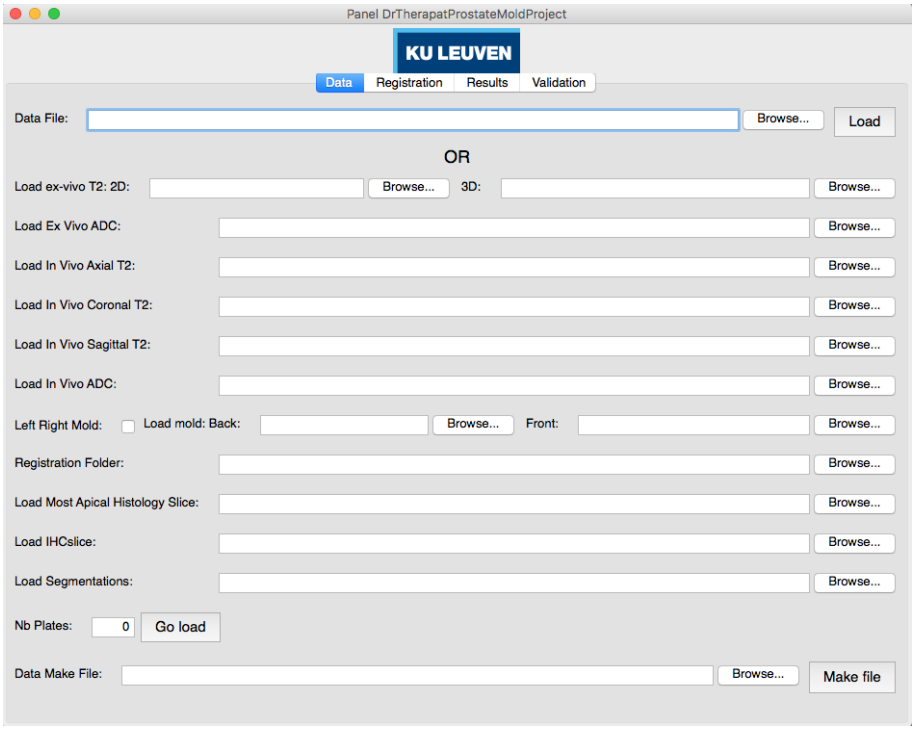

FIGURE A.1: Interface of the DrTherapat tool with its data, registration, results and validation tab.

Ex-vivo to in-vivo

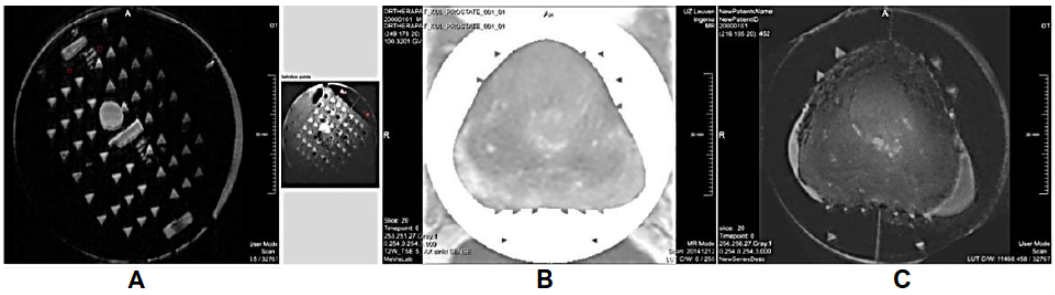

Figure A.2: **A**: indication of back landmarks of the mold and its lower side. **B**: in-vivo T2w-image overlaid with prostate mold. **C**: finding matching slices on the ex-vivo T2w-image and exclude distorted slices. Adapted from [34].

Macroblock to in-vivo

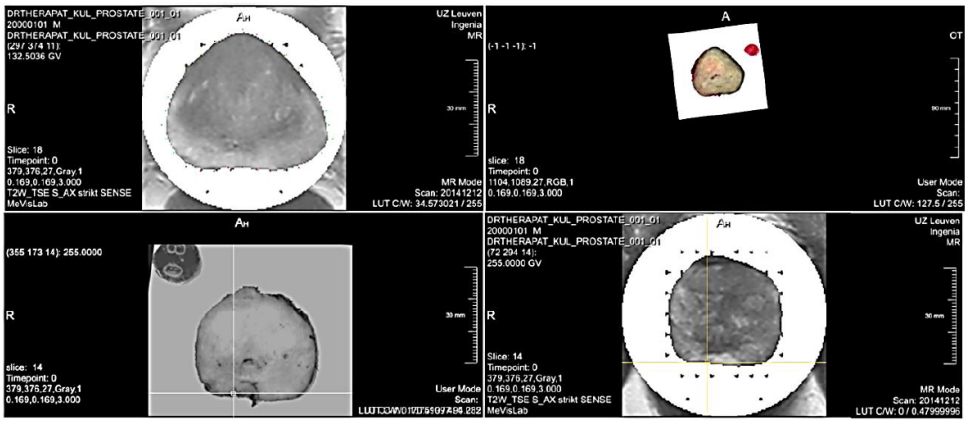

Figure A.3: Visual selection of corresponding slices based on pathologic indications on the cutting-template paper. Adapted from [34].

Tumor segmentation and histology to ex-vivo

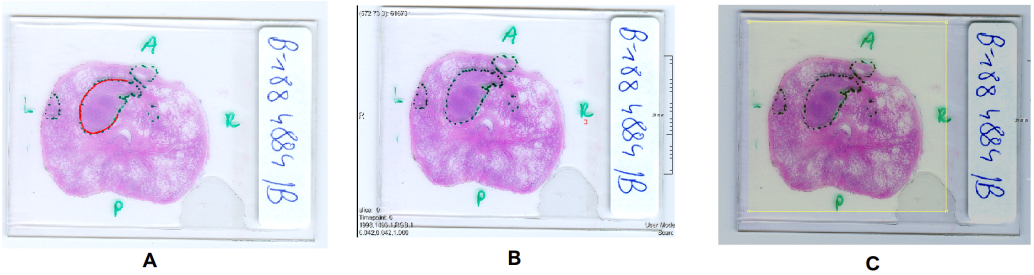

FIGURE A.4: **A**: manual tumor delineation. **B**: indication of the right and anterior of each histology slice. **C**: ROI selection around the histological tissue. Note that the steps for registration of histology to macroblocks are not shown here, since these steps were not implemented in the thesis.

Functional images

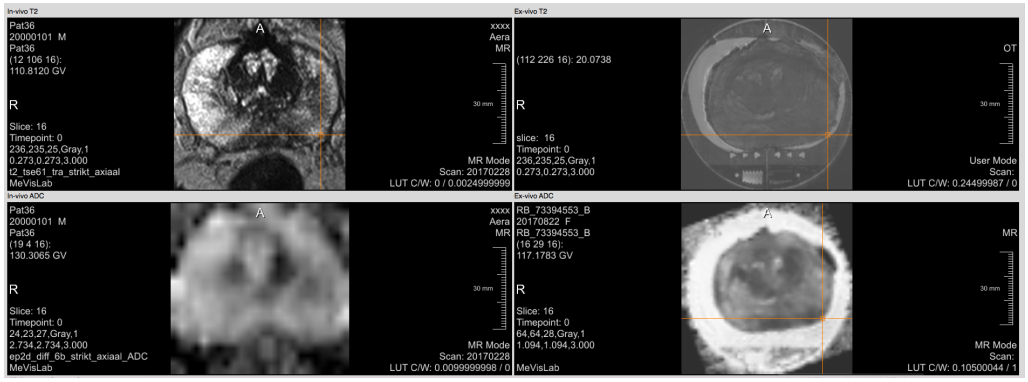

FIGURE A.5: For the additional functional images, the registration to the in-vivo space could be done by simply applying the transformation found in the 'Ex-vivo to in-vivo' step.

Generation of segmentations for control tissue

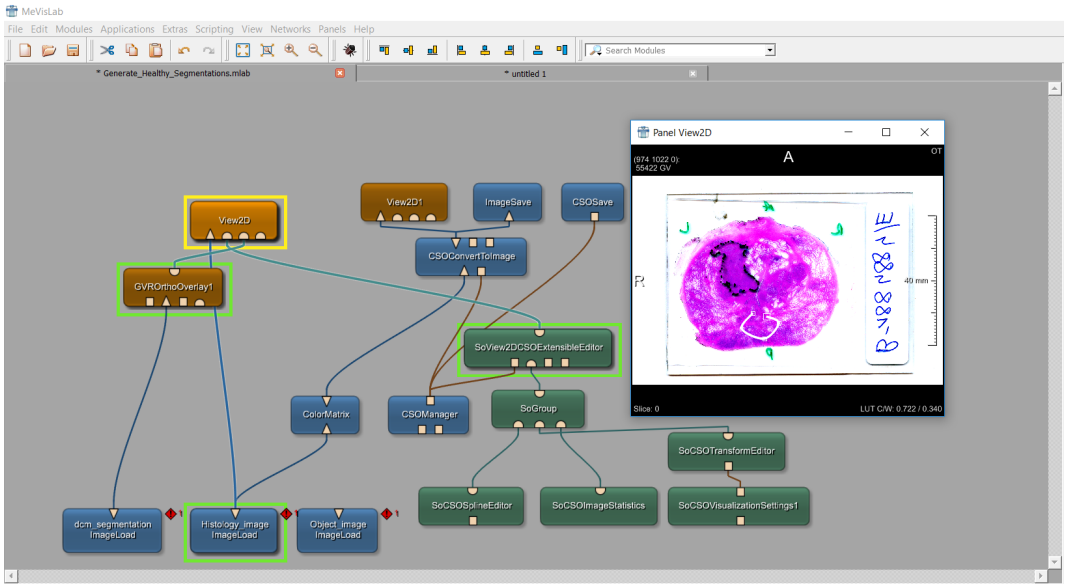

Figure A.6: Illustration of the MeVislab tool for generation of segmentations for control tissue.

Labeling of segmentations

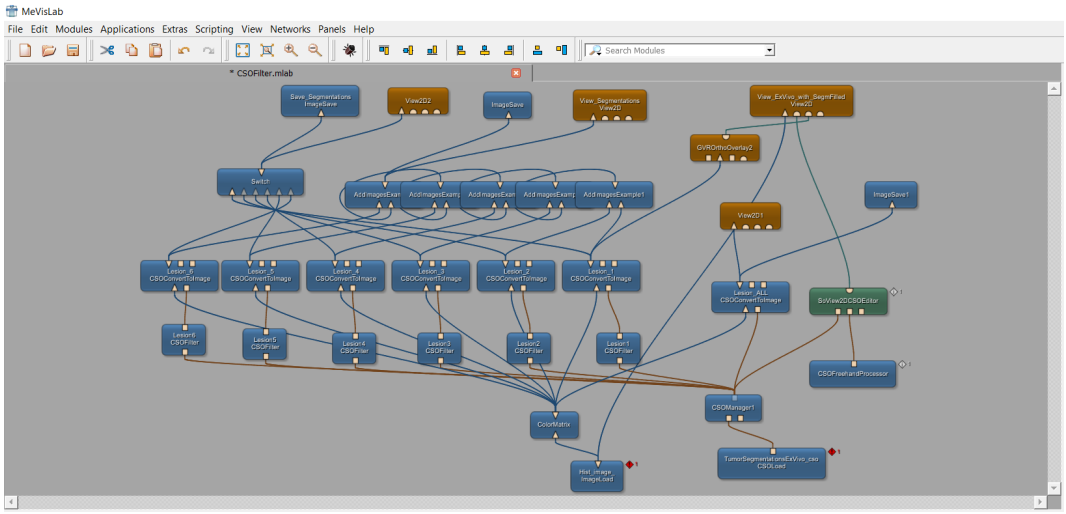

Figure A.7: Illustration of the MeVislab tool for labeling the segmentations.

Appendix B

Patient numbering within DrTherapat database

TABLE B.1: Identification of the data set used in this thesis within the DrTherapat database.

Patient numbering in thesis	Patient numbering within DrTherapat
1	21
2	22
3	25
4	28
5	29
6	30
7	33
8	35
9	36
10	37
11	38
12	40
13	43
14	45
15	46

Appendix C

Illustrations of registered, segmented object images

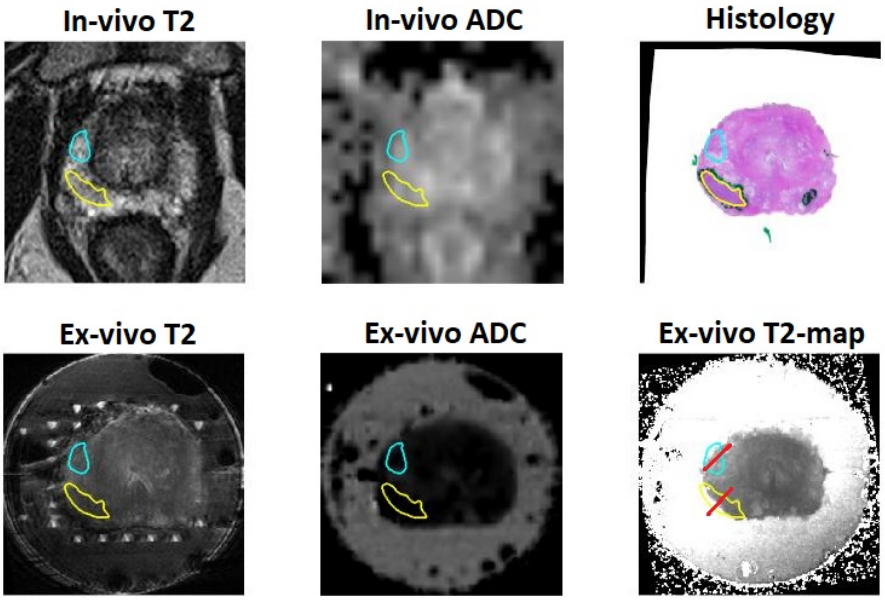

FIGURE C.1: Registered object images overlaid with the corresponding segmentations for slice 14 of patient 4. Tumor segmentations are yellow, control segmentations cyan. Excluded regions are crossed out with a red line.

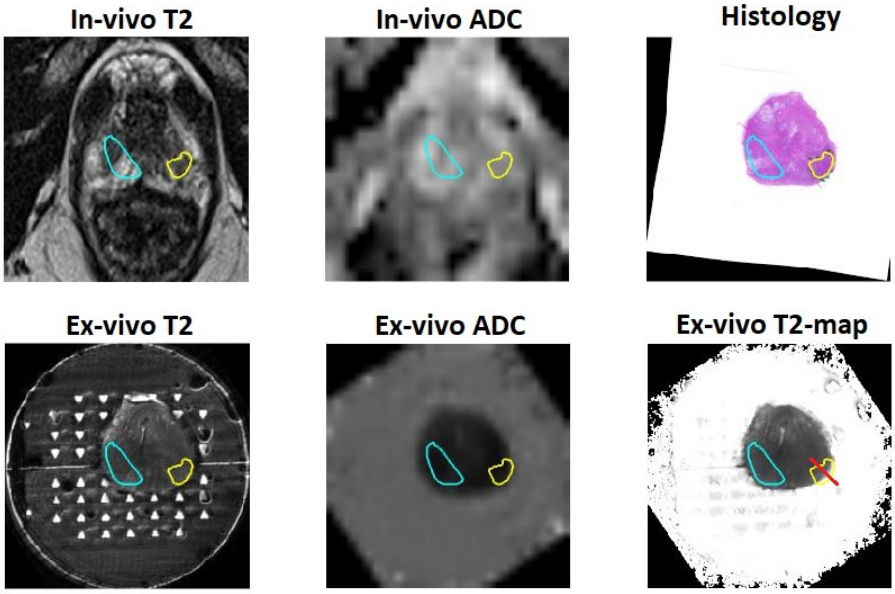

Figure C.2: Registered object images overlaid with the corresponding segmentations for slice 13 of patient 7. Tumor segmentations are yellow, control segmentations cyan. Excluded regions are crossed out with a red line.

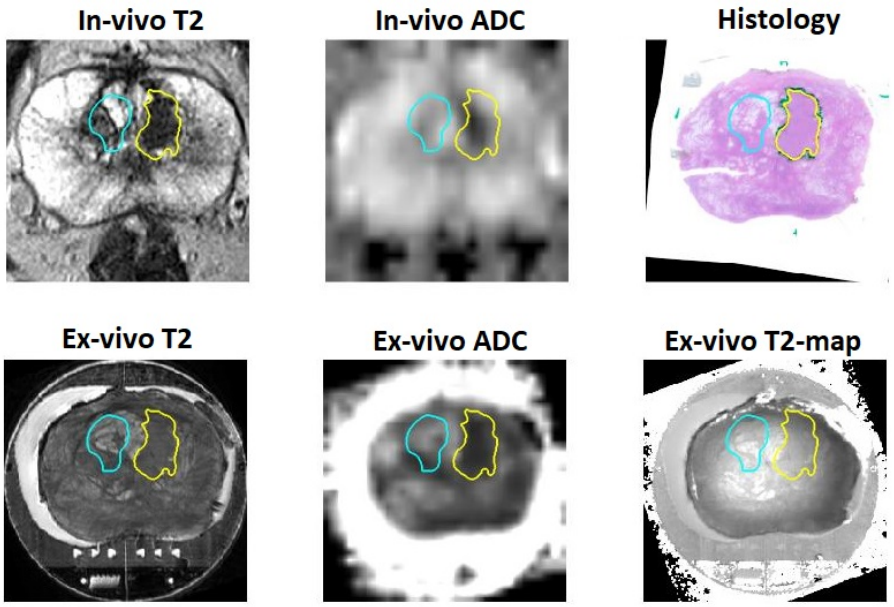

Figure C.3: Registered object images overlaid with the corresponding segmentations for slice 16 of patient 9. Tumor segmentations are yellow, control segmentations cyan.

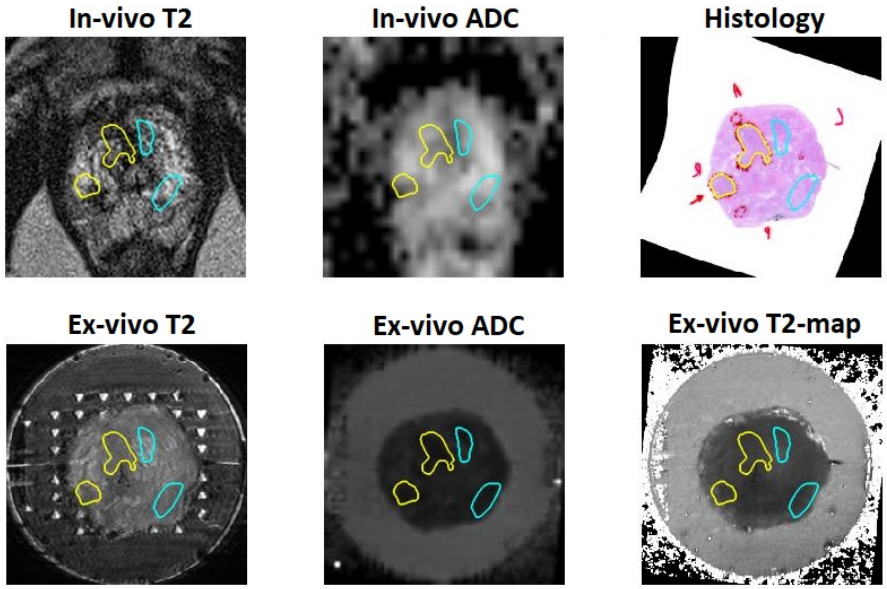

FIGURE C.4: Registered object images overlaid with the corresponding segmentations for slice 11 of patient 10. Tumor segmentations are yellow, control segmentations cyan.

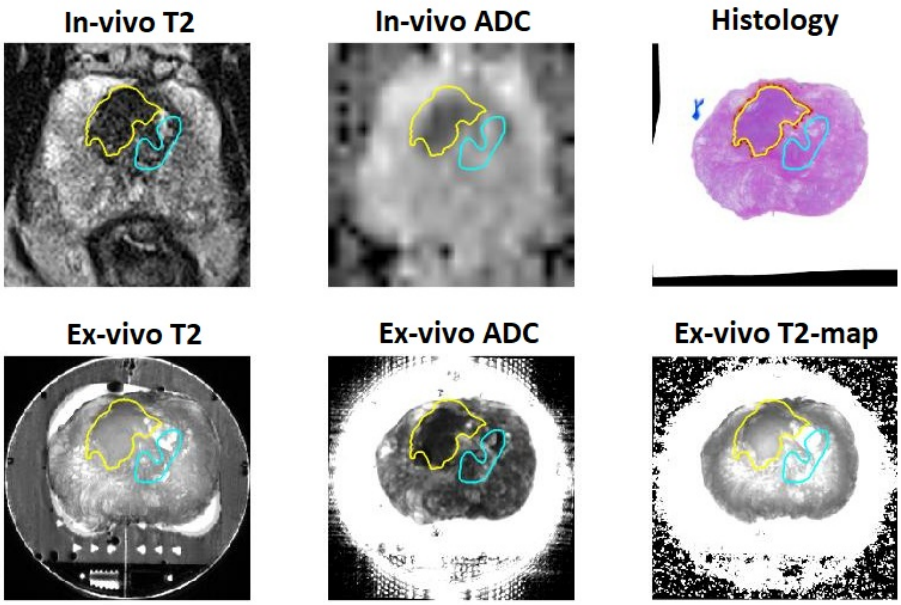

FIGURE C.5: Registered object images overlaid with the corresponding segmentations for slice 18 of patient 12. Tumor segmentations are yellow, control segmentations cyan.

Bibliography

[1] Centers for disease control and prevention [internet]. Atlanta: CDC. Cancer Among Men; 2017 Jun 5 [cited Jan 16 2017]. Available from: https://www.cdc.gov/cancer/dcpc/data/men.htm

[2] NIH National Cancer Institute [internet]. Bethesda: NIH. Prostate Cancer-Patient Version; 2018 Feb 26 [cited April 3 2018]. Available from: https://www.cancer.gov/types/prostate

[3] American Cancer Society [internet]. US: American Cancer Society. Key Statistics for Prostate Cancer; 2017 Jan 5 [cited Oct 19 2017]. Available from: https://www.cancer.org/cancer/prostate-cancer/about/key-statistics.html

[4] GLOBOCAN [internet]. Geneva: World Health Organization. Prostate cancer estimated incidence, mortality and prevalence worldwide in 2012; 2012 [cited May 14 2018]. Available from: http://globocan.iarc.fr/old/FactSheets/cancers/prostate-new.asp

[5] Michael A. Jacobs, Ronald Ouwerkerk, Kyle Petrowski, Katarzyna J. Macura. Diffusion weighted imaging with ADC mapping and spectroscopy in prostate cancer. TMRI. 2008 Dec; 19(6): 261−272

[6] World Cancer Research Fund International [internet]. London: World Cancer Research Fund International. Prostate cancer statistics; 2015 Jan 16 [cited Oct 19 2017]. Available from: http://www.wcrf.org/int/cancer-facts-figures/data-specific-cancers/prostate-cancer-statistics

[7] An Elen, Sofie Isebaert, Frederik De Keyzer, Uwe Himmelreich, Steven Joniau, Lorenzo Tosco, et al. Validation of an improved prostate mold design for registration of in-vivo and ex-vivo MRI to histology. CLIP. 2016 Sep; 36-43

[8] Roger M. Bourne, Colleen Bailey, Edward William Johnston, Hayley Pye, Susan Heavey, Hayley Whitaker, et al. Apparatus for Histological Validation of In Vivo and Ex Vivo Magnetic Resonance Imaging of the Human Prostate. Front Oncol. 2017 Mar; 7:47

[9] WebMD [image on internet]. Atlanta: Matthew Hoffman. Picture of the Prostate; 2017 Mar 11 [cited Oct 17 2017]. Available from: https://www.webmd.com/urinary-incontinence-oab/picture-of-the-prostate#2

[10] UpToDate [image on internet]. UpToDate. Zones of the prostate gland; 2011 [cited Dec 27 2017]. Available from: http://cursoenarm.net/UPTODATE/contents/mobipreview.htm?39/39/40569

[11] MedScape [internet]. US: Nicolas A Muruve. Prostate Anatomy; 2017 Sep 13 [cited Dec 27 2017]. Available from: https://emedicine.medscape.com/article/1923122-overview#a2

[12] LiveScience [internet]. US: Molika Ashford. What Does the Prostate Gland Do?; 2010 Aug 09 [cited Dec 27 2017]. Available from: https://www.livescience.com/32751-what-does-the-prostate-gland-do.html

[13] WebMD [internet]. Atlanta: E. Gregory Thompson. Digital Rectal Examination (DRE); 2015 Nov 20 [cited Oct 16 2017]. Available from: https://www.webmd.com/colorectal-cancer/digital-rectal-examination-dre#1

[14] Cancer research UK [internet]. UK: Cancer research UK. Transrectal ultrasound guided (TRUS) biopsy; 2016 Jul 6 [cited Oct 17 2017]. Available from: http://www.cancerresearchuk.org/about-cancer/prostate-cancer/getting-diagnosed/tests-diagnose/transrectal-ultrasound-guided-trus-biopsy

[15] American Cancer Society [internet]. US: American Cancer Society. Prostate Cancer Stages; 2016 Mar 11 [cited Oct 17 2017]. Available from: https://www.cancer.org/treatment/understanding-your-diagnosis/staging.html

[16] MedScape [internet]. US: Natasza M Posielski. Prostate Cancer Staging; 2017 Oct 04 [cited Dec 28 2017]. Available from: https://emedicine.medscape.com/article/2007051-overview

[17] Prostaat.be [internet]. Gleasonscore; 2013 [cited Oct 17 2017]. Available from: http://www.prostaat.be/prostaatkanker/diagnose/gleason-score/

[18] Prostate cancer UK [internet]. UK: Prostate cancer UK. The PSA test; 2016 Nov [cited Dec 28 2017]. Available from: https://prostatecanceruk.org/prostate-information/prostate-tests/psa-test

[19] MedicalNewsToday [internet]. UK: Christian Nordqvist. Prostate cancer in detail; 2017 Nov 27 [cited Dec 4 2017]. Available from: https://www.medicalnewstoday.com/articles/150086.php

[20] American Cancer Society [internet]. US: American Cancer Society. Treating Prostate Cancer; 2016 Feb 16 [cited Dec 4 2017]. Available from: https://www.cancer.org/cancer/prostate-cancer/treating.html

[21] CaseMed [internet]. David C Preston, MD. Magnetic Resonance Imaging (MRI) of the Brain and Spine: Basics; 2006 30 Nov [cited Dec 29 2017]. Available from: http://casemed.case.edu/clerkships/neurology/Web%20Neurorad/MRI%20Basics.htm

[22] OTpedia [internet]. OTpedia. Localizer (scout) images; [cited May 16 2018]. Available from: http://www.otpedia.com/entryDetails.cfm?id=398

[23] Paul Suetens. Fundamentals of Medical Imaging. 2nd ed. US: Cambridge University Press. 2009. 253 p.

[24] John V. Hegde BS, Robert V. Mulkern PhD, Lawrence P. Panych PhD, Fiona M. Fennessy MD PhD, Andriy Fedorov PhD, Stephan E. Maier MD PhD, et al. Multiparametric MRI of prostate cancer: an update on state-ofthe- art techniques and their performance in detecting and localizing prostate cancer. JMRI. 2013 May. 37(5): 1035-1054

[25] Sangeet Ghai and Masoom A. Haider. Multiparametric-MRI in diagnosis of prostate cancer. Indian J Urol. 2015 Jul-Sep. 31(3): 194-201.

[26] Junqian Xu, Peter A. Humphrey, Adam S. Kibel, Abraham Z. Snyder, Vamsidhar R. Narra, Joseph J.H. Ackerman et al. Magnetic resonance diffusion characteristics of histologically defined prostate cancer in humans. Magn Reson Med. 2009 Apr. 61(4): 842-850

[27] Carlos F. Uribe, Edward C. Jones, Silvia D. Chang, S. Larry Goldenberg, Stefan A. Reinsberg, Piotr Kozlowski. In vivo 3T and ex vivo 7T diffusion tensor imaging of prostate cancer: correlation with histology. MRI. 2015 Feb 18. 33 577-583

[28] Elastix [internet]. Stefan Klein and Marius Staring. Elastix; Mar 29 2018 [cited May 21 2018]. Available from: http://elastix.isi.uu.nl/

[29] H. M. Reynolds, S. Williams, A. Zhang, R. Chakravorty, D. Rawlinson, C. S. Ong et al. Development of a registration framework to validate MRI with histology for prostate focal therapy. Med Phys. 2015 Nov 19. 42 (12)

[30] Alan Priester, Shyam Natarajan, Jesse D Le, James Garritano, Bryan Radosavcev, Warren Grundfest et al. A system for evaluating magnetic resonance imaging of prostate cancer using patient-specific 3D printed molds. Am J Clin Exp Urol. 2014 Jul 15. 2(2):127-135

[31] Greetje Groenendaal M.Sc., Alie Borren M.D., Maaike R. Moman Ph.D., Evelyn Monninkhof Ph.D., Paul J. van Diest Ph.D., Marielle E.P. Philippens Ph.D., et al. Pathologic validation of a model based on diffusion-weighted imaging and dynamic contrast-enhanced magnetic resonance imaging for tumor delineation in the prostate peripheral zone. Int J Radiation Oncol Biol Phys. 2011 Jul 18. Vol. 82, No. 3, pp. e537ee544

[32] Asha Singanamalli, Rachel Sparks, Mirabela Rusu, Natalie Shih, Amy Ziober, John Tomaszewski, et al. Identifying in vivo DCE MRI parameters correlated with ex vivo quantitative microvessel architecture: a radiohistomorphometric approach. Proc. SPIE 8676, Medical Imaging 2013: Digital Pathology. 2013 Mar 29. 867604

[33] Sofie Isebaert PhD, Laura Van den Bergh MD, Karin Haustermans MD, PhD, Steven Joniau MD, Evelyne Lerut MD, PhD, Liesbeth De Wever, et al. Multiparametric MRI for prostate cancer localization in correlation to whole-mount histopathology. JMRI. 2013 Jun. 37(6):1392-401

[34] Mary Glorieux. Virtual pathology of prostate cancer samples using MRI. 2016.

[35] Warren D. Foltz, Supriya Chopra, Peter Chung, Andrew Bayley, Charles Catton, David Jaffray et al. Clinical prostate T2 quantification using magnetization-prepared spiral imaging. Magn Reson Med. 2010. 64:1155-1161

[36] Wei Liu, D.Sc, Baris Turkbey, M.D, Julien Senegas, Ph.D, Stefanie Remmele, Ph.D, Sheng Xu, Ph.D, Jochen Kruecker, Ph.D et al. Accelerated T2 mapping for characterization of prostate cancer. Magn Reson Med. 2011 May. 65(5): 1400-1406

[37] Joseph R. Roebuck, Steven J. Haker, Dimitris Mitsouras, Frank J. Rybicki1, Clare M. Tempany, and Robert V. Mulkern. Carr-Purcell-Meiboom-Gill (CPMG) imaging of prostate cancer: quantitative T2 values for cancer discrimination. Magn Reson Imaging. 2009 May. 27(4): 497-502

[38] G. J. Metzger, PhD, C. Kalavagunta, PhD, B. Spilseth, MD, P. J. Bolan, PhD, X. Li, PhD, D. Hutter, et al. Development of quantitative multiparametric MRI models for prostate cancer detection using registered correlative histopathology. Radiology. 2016 June. 279(3): 805-816

[39] Roger M. Bourne, Nyoman Kurniawan, Gary Cowin, Timothy Stait-Gardner, Paul Sved, Geoffrey Watson, et al. Biexponential diffusion decay in formalin-fixed prostate tissue: preliminary findings. Magn Reson Med. 2012 Sep. 68:954−959

[40] Roger M. Bourne, Nyoman Kurniawan, Gary Cowin, Timothy Stait-Gardner, Paul Sved, Geoffrey Watson, et al. Microscopic diffusivity compartmentation in formalin-fixed prostate tissue. Magn Reson Med. 2012 Aug. 68:614−620

[41] M. A. Jacobs, V. Chacko, B. Okollie, T. Lotan and K. J. Macura. Can ex-vivo MRI be used for correlating diffusion weighted imaging parameters to pathology for validation of in-vivo multiparametric MRI. Proc Intl Soc Mag Reson Med. 2010. 18

[42] A. Hoang Dinh, R. Souchon, C. Melodelima, F. Bratan, F. Mege-Lechevallier, M. Colombel, et al. Characterization of prostate cancer using T2 mapping at 3 T: A multi-scanner study. Diagnostic and Interventional Imaging. 2015. 96, 365-372.

[43] Flavie Bratan, Emilie Niaf, Christelle Melodelima, Anne Laure Chesnais, Remi Souchon, Florence Mege-Lechevallier, et al. Influence of imaging and histological factors on prostate cancer detection and localisation on multiparametric MRI: a prospective study. Eur Radiol. 2013. 23:2019-2029.

[44] Yousef Mazaheri, H. Alberto Vargas, Gregory Nyman, Oguz Akin, and Hedvig Hricak. Image artifacts on prostate diffusion-weighted magnetic resonance imaging: trade-offs at 1.5 Tesla and 3.0 Tesla. Acad Radiol. 2013 August. 20(8): 1041-1047

[45] Andrew B. Rosenkrantz, MD, Marcel Oei, MD, James S. Babb, PhD, Benjamin E. Niver, BA, and Bachir Taouli, MD. Diffusion-weighted imaging of the abdomen at 3.0 Tesla: image quality and apparent diffusion coefficient reproducibility compared with 1.5 Tesla. JMRI. 2011. 33:128-135

[46] Roger Bourne, Andre Bongers, Ned Charles, Carl Power, Paul Sved, and Geoffrey Watson. Effect of formalin fixation on biexponential modeling of diffusion decay in prostate tissue. Magn Reson Med. 2013 Oct. 70(4):1160−6

[47] C. R. Haney, X. Fan, G. Agrawal, C. A. Pelizzari, G. S. Karczmar, J. Bakst, et al. High resolution ex vivo MRI of prostate specimen, correlation with whole-mount histology and in vivo MRI. Proc. Intl. Soc. Mag. Reson. Med. 2011. 19

[48] Siemens. SIEMENS MAGNETOM Aera syngo MR D13. 2014 Jun 27. pp1-31.

[49] International Society for Sexual Medicine [internet]. ISSM, Netherlands. What is robotic-assisted laparoscopic prostatectomy (RALP)?. [cited Apr 5 2018]. Available from: http://www.issm.info/sexual-health-qa/what-is-robotic-assisted-laparoscopic-prostatectomy-ralp/

[50] Bruker, Biospec [internet]. Bruker, Germany. General Specifications. [cited Apr 8 2018]. Available from: https://www.bruker.com/products/mr/preclinical-mri/biospec/technical-details.html

[51] Warwick [internet]. Peter James Ros, UK; Dec 3 2012 RARE. [cited Apr 8 2018]. Available from: https://warwick.ac.uk/fac/sci/physics/research/condensedmatt/imr_cdt/students/peter_james_ross/rapidimaging/rare/

[52] Wikipedia [internet]. Wikipedia. Fast low angle shot magnetic resonance imaging; Feb 1 2018 [cited Apr 8 2018]. Available from: https://en.wikipedia.org/wiki/Fast_low_angle_shot_magnetic_resonance_imaging

[53] Bruker, Biospec. Paravision manual chap A05: Applications. pp71-88 and 126-132

[54] SourceForge [internet]. Matthew Brett. pvconv.pl - a Bruker data converter; Oct 10 2007 [cited May 16 2018]. Available from: http://pvconv.sourceforge.net/

[55] Dicom standard [internet]. DICOM. Key concepts; [cited Apr 9 2018]. Available from: https://www.dicomstandard.org/concepts/

[56] Wikipedia [internet]. Wikipedia. Analyze (imaging software); Sep 1 2016 [cited Apr 9 2018]. Available from: https://en.wikipedia.org/wiki/Analyze_(imaging_software)

[57] Wikipedia [internet]. Wikipedia. Tagged Image File Format; Mar 28 2017 [cited Jun 3 2018]. Available from: https://nl.wikipedia.org/wiki/Tagged_Image_File_Format

[58] Research portal Kuleuven [internet]. Kuleuven. Digital radiation therapy patient. (3E130200); 2016 [cited May 21 2018]. Available from: https://www.kuleuven.be/onderzoek/portaal/#/projecten/3E130200?lang=en&hl=en

[59] KuLeuven. An Elen. DrTherapatProstateMoldProject: Tool Manual.

[60] Alie Borren, Maaike R. Moman, Greetje Groenendaal, Arto E. Boeken Kruger, Paul J. van Diest, Petra van der Groep, et al. Why prostate tumour delineation based on apparent diffusion coefficient is challenging: an exploration of the tissue microanatomy. Acta Oncologica. Apr 28 2013. 52:8, 1629-1636

[61] University of Virginia library [internet]. Clay Ford. The Wilcoxon Rank Sum Test; Jan 5 2017 [cited May 22 2018]. Available from: https://data.library.virginia.edu/the-wilcoxon-rank-sum-test/

[62] Paul Tofts. Proton density of tissue water. John Wiley & Sons. 2003.

[63] Questions and answers in MRI [internet]. Allen D. Elster, MD. Relaxation & Field Strength; [cited May 26 2018]. Available from: http://mri-q.com/bo-effect-on-t1–t2.html

[64] Roman Sosnowski, Magdalena Zagrodzka and Tomasz Borkowski. The limitations of multiparametric magnetic resonance imaging also must be borne in mind. Cent European J Urol. 2016. 69(1): 22-23.

[65] Wikipedia [internet]. Wikipedia. Immunohistochemistry; May 16 2018. [cited Jun 3 2018]. Available from: https://en.wikipedia.org/wiki/Immunohistochemistry

[66] Rakesh Shiradkar , Tarun K Podder, Ahmad Algohary, Satish Viswanath, Rodney J. Ellis and Anant Madabhushi. Radiomics based targeted radiotherapy planning (Rad-TRaP): a computational framework for prostate cancer treatment planning with MRI. Radiation Oncology. 2016. 11:148

[67] Patrik Brynolfsson, David Nilsson, Turid Torheim, Thomas Asklund, Camilla Thellenberg Karlsson, Johan Trygg, et al. Haralick texture features from apparent diffusion coefficient (ADC) MRI images depend on imaging and pre-processing parameters. Scientific Reports. June 22 2017. 7: 4041